Biomaterials 334 (2026) 124256

Contents lists available at ScienceDirect

Biomaterials

journal homepage: www.elsevier.com/locate/biomaterials

Hide-and-seek molecular navigator targets tumor cell surface thiols by programmable disulfide exchange

Pengwen Chen [a], Guanghao Hu [a], Wenqian Yang [a], Yuki Nakashima [a], Zhining Xu [b,c], Yiyi Yang [d,e], Soichiro Kondo [a], Xiwen Chen [a], Sosuke Takasugi [a], Ervin Kovács [b], Katsuhito Fujiu [d,e,f], Horacio Cabral [a,*]

[a] Department of Bioengineering, Graduate School of Engineering, The University of Tokyo, 7-3-1 Hongo, Bunkyo-ku, Tokyo, 113-0033, Japan
[b] Institute of Materials and Environmental Chemistry, HUN-REN Research Centre for Natural Sciences, 1117, Magyar Tudósok Körútja 2, Budapest, Hungary
[c] Hevesy György PhD School of Chemistry, Eötvös Loránd University, 1053, Egyetem tér 1–3, Budapest, Hungary
[d] Department of Cardiovascular Medicine, The University of Tokyo, 7-3-1 Hongo, Bunkyo-ku, Tokyo, 113-0033, Japan
[e] Department of Advanced Cardiology, The University of Tokyo, 7-3-1 Hongo, Bunkyo-ku, Tokyo, 113-0033, Japan
[f] Department of Integrative Physiology, Institute of Science Tokyo, 1-5-45 Yushima, Bunkyo-ku, Tokyo, 113-8510, Japan

ARTICLE INFO

Keywords:
Disulfide exchange
Drug delivery
Albumin hitchhiking
Antitumor therapeutics
Immunogenic cell death

ABSTRACT

Metabolism dysregulation induces distinct thiol profiles between cancer and healthy cells, offering an attractive therapeutic target. However, systemically targeting cancer-specific thiols remains challenging due to the widespread presence of these groups in the physiological environment. Here, we design a molecular navigator (MONA) with spatiotemporally programmable thiol-reactivity to target the thiols on cancer cells upon intravenous injection. MONA operates through a bioresponsive "Hide-and-Seek" mechanism based on tunable disulfide exchange across biological compartments. In the "Hide" phase, MONA circulates stealthily through rapid conjugation with endogenous albumin *via* disulfide bonding. In the "Seek" phase, albumin facilitates MONA transcytosis into tumors, where elevated glutathione levels trigger disulfide exchange, releasing MONA to multivalently engage with thiols on cancer cells. When conjugated with a photosensitizer, MONA induces cancer cell membrane disruption upon light irradiation, enabling potent phototherapy. This approach leads to complete tumor regression and systemic abscopal effects in an immunosuppressive murine breast cancer model. These findings highlight MONA as a powerful strategy for precise thiol-targeted cancer therapy.

1. Introduction

Dysregulated redox metabolism is a hallmark of cancer [1]. Altered expression profile of redox-regulating enzymes, such as protein disulfide isomerase (PDI) and components of the thioredoxin system [2–4], shifts the redox balance in cancer cells [5,6]. Notably, disruption of redox homeostasis on cell membrane perturbs the thiol-disulfide equilibrium, leading to an upregulation of activate thiols on the cell membrane [7,8]. These membrane-associated thiols play critical roles in various cellular processes, including regulation of cellular signaling pathways [9,10], cell proliferation [11], and promotion of cell adhesion, migration, and metastasis [7,8]. Thus, membrane thiols represent a distinctive molecular signature that can be exploited for selective cancer diagnosis, targeted therapy, and drug delivery [8,12–14].

Systemic targeting of this molecular signature is strongly limited by physiological thiol chemistry. Circulating thiols, particularly the Cys34 group of serum albumin which comprises approximately 80% of the total free thiols in plasma [15–18], act as a dominant sink for thiol-reactive agents [19], while thiols on healthy tissues introduce further off-target risks [20]. A "Hide-and-Seek" design, in which thiol reactivity is concealed in circulation and revealed only within the tumor to engage its target, can circumvent these barriers. Dynamic disulfide linkages provide a potential mechanism for such control [21,22]. Specifically, reactive warheads can be cloaked as disulfide conjugates on bulky albumin, shielding their activity and extending plasma residence [21]. Once at the tumor site, locally elevated glutathione (GSH) levels can drive rapid thiol-disulfide exchange [22], removing the albumin cloak and releasing the active species *in situ*. Yet, detachment alone does not guarantee targeting, as the warhead must selectively rebind to the thiols on cancer cells amid abundant competing thiols. To our

* Corresponding author.
E-mail address: horacio@bmw.t.u-tokyo.ac.jp (H. Cabral).

https://doi.org/10.1016/j.biomaterials.2026.124256
Received 5 February 2026; Received in revised form 7 April 2026; Accepted 27 April 2026
Available online 30 April 2026

knowledge, no strategy has succeeded in distinguishing these thiol pools within the tumor microenvironment (TME), as doing so requires an unprecedented level of molecular precision and finely tuned exchange kinetics.

Here, we report a smart molecular navigator (MONA) that executes a "Hide-and-Seek" program to target cancer cell thiols *via* controlled disulfide exchange dynamics (Scheme 1). MONA was constructed by screening candidates with different polypeptide backbones, including cationic poly(L-Lysine) (pLL) and anionic poly(L-aspartic acid) (pAsp), modified with pyridyl disulfide (PDS) group, a safe and biocompatible thiol-reactive moiety that has been widely reported in biomaterial systems [14]. This design creates distinct local charges surrounding the PDS groups precisely tuning disulfide exchange reactions [22–25]. Critically, the PDS multivalency of MONA allows selectively engaging thiol pools in the GSH-rich TME, promoting high avidity binding to dense thiol arrays on cancer cell surfaces, while soluble monovalent competitors like albumin dissociate rapidly. The pLL-based MONA displayed rapid disulfide exchange process *in vitro* and *in vivo*, enabling reversible albumin conjugation in circulation and GSH-triggered dynamics in tumors. To showcase the functional utility, we conjugated MONA with a photosensitizer, enabling selective membrane damage and light-induced immunogenic cell death (ICD) [26–30]. Remarkably, a single intravenous (i.v.) dose followed by light irradiation eradicated immunosuppressive orthotopic triple negative breast cancer (TNBC) tumors and

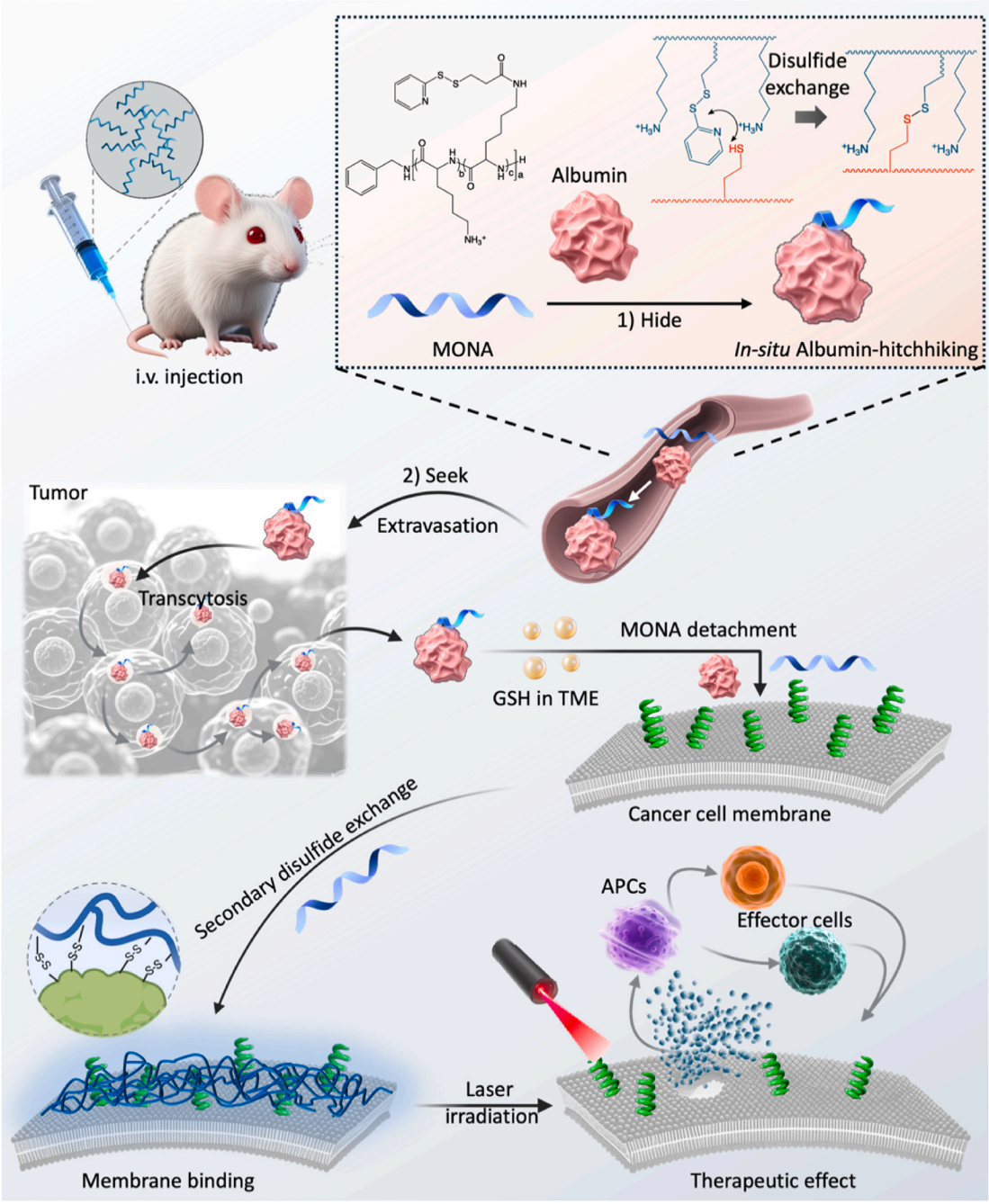

Scheme 1. Schematic illustration showing the working mechanism of MONA system. Upon systemic injection, MONA binds to albumin by disulfide linkage. This albumin hitchhiking mechanism ensures stable blood circulation and effective intratumoral accumulation. After the albumin-MONA complex reaches TME, the enriched GSH can mediate the disulfide exchange to transfer the polymers from albumins to cancer cell membrane. Light irradiation then activates the photosensitizer and induces membrane rupture to initiate ICD for evoking antitumoral immune responses.

elicited a robust abscopal effect. These findings establish a redox-guided molecular design that transforms systemic delivery challenges into precise strategies for selective cancer cell surface engagement.

2. Results

2.1. PDS-modified polypeptides bind to albumin reversibly

A series of polypeptides were synthesized (Supplementary Scheme S1-2 and Supplementary Figure S1-6). For pLL, two chain lengths with 25 and 50 lysine blocks were prepared, denoted as pLL_{25} and pLL_{50}. A pAsp backbone comprising 25 units ($pAsp_{25}$) was also synthesized. PDS groups were subsequently conjugated to the side chains of these polypeptides to generate MONA candidates (Fig. 1A). Confirmed by NMR spectra and colorimetric analysis, pLL_{25}, pLL_{50}, and $pAsp_{25}$ backbones were modified with 8, 11, and 7 PDS groups per polymer, respectively. All these polymers could be stably dispersed in aqueous solutions (Supplementary Figure S7). These formulations are thus referred to as $pLL_{25}(PDS)_8$, $pLL_{50}(PDS)_{11}$ and $pAsp_{25}(PDS)_7$. The distinct polymer backbones of pLL and pAsp provide different neighboring environments for the PDS groups in MONA. In pLL-based MONA, the PDS groups are surrounded by amino groups, whereas in pAsp-based MONA, they are surrounded by carboxylic acids.

To assess the ability of the MONA candidates to bind albumin, a fluorescence resonance energy transfer (FRET) assay was employed. Cy3-labeled bovine serum albumin (BSA) and Cy5-labeled polymers

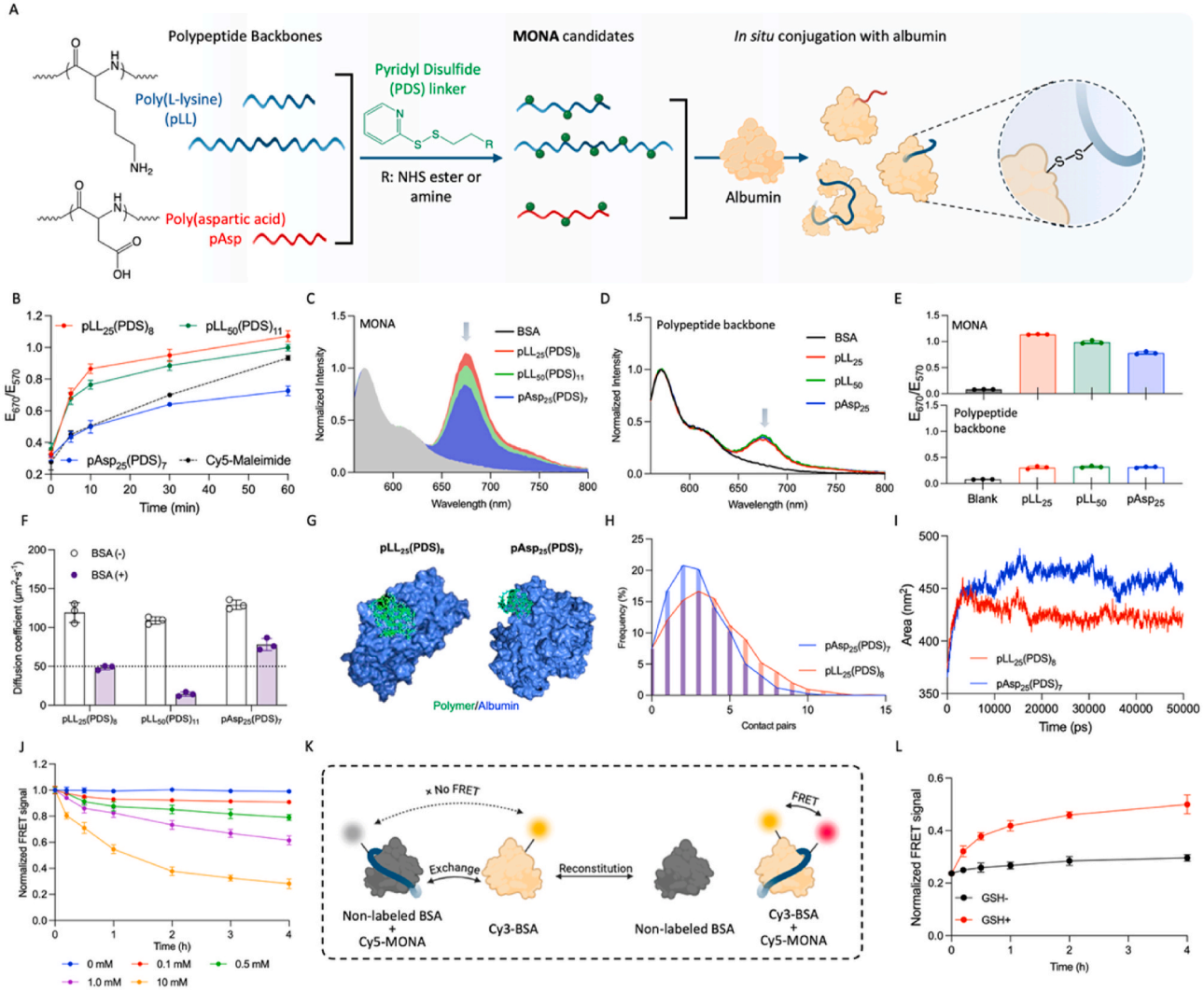

Fig. 1. PDS-modified polypeptides bind to albumin reversibly. A. Schematic illustration showing the design of MONA and the mechanism of albumin binding. MONA candidates were constructed by conjugating PDS groups to polypeptide backbones. The PDS groups can react with the Cys34 thiol of albumin. By choosing optimal polypeptide backbone structure and length, efficient complexation between MONA and albumin can be achieved. **B.** Quantified FRET signals (ratio of emission intensities at 675 to 570 nm, E_{675}/E_{570}) from the mixture of Cy3-labeled BSA and Cy5-labeled polymers incubated under 37 °C. Data were plotted as the mean ± S.D., $n = 3$ measurements. **C.** Emission spectra of the mixtures of BSA and MONAs after 12 h incubation (excitation wavelength: 550 nm). The arrow indicates the peak indicating FRET emission. **D.** Emission spectra of the mixtures of BSA and polymer backbones after 12 h incubation (excitation wavelength: 550 nm). **E.** Quantified E_{670}/E_{570} ratios from BSA + polymer mixtures after 12 h incubation. Data were plotted as the mean ± S.D., $n = 3$ measurements. **F.** Diffusion coefficients of the samples quantified by the FCS measurements. The dashed line indicates the diffusion coefficient of BSA measured in the experiment (≈50 $\mu m^2 s^{-1}$). Data were plotted as the mean ± S.D., $n = 3$ measurements. **G.** Snapshot showing the conformation of polymers associating with albumin at the end point of MD simulation. **H.** Frequency of atom contact pair numbers between polymers and albumin during the simulation period. **I.** SASA change of the systems during simulation period. **J.** FRET signal change of the $pLL_{25}(PDS)_8$+BSA mixture after dissolving into buffers with different GSH concentration. Data were plotted as the mean ± S.D., $n = 3$ measurements. **K.** Experiment confirming the disulfide exchange process inducing the switch of pLL(PDS) binding targets. Cy5-labeled $pLL_{25}(PDS)_8$ was pre-mixed with non-labeled BSA, then treated with Cy3-labeled BSA. **L.** The FRET signals of the samples measured during the experiment. Data were plotted as the mean ± S.D., $n = 3$ measurements.

were mixed in phosphate buffer (10 mM, pH 7.4), and the emission spectra were recorded under 550 nm excitation. The FRET signal was defined as the ratio of fluorescence intensities at 670 nm and 570 nm (E_{670}/E_{570}). All PDS-modified polypeptides exhibited an increase in FRET signal upon mixing with Cy3-labeled BSA (Fig. 1B), indicating binding between the polymers and BSA. Compared to $pLL_{25}(PDS)_8$ and $pLL_{50}(PDS)_{11}$, $pAsp_{25}(PDS)_7$ showed both a slower increase in the FRET signal and a lower overall FRET intensity after prolonged incubation (12 h) (Fig. 1C), suggesting slower binding kinetics and reduced affinity towards BSA. This difference likely arises from the local charge condition surrounding the disulfide groups, which influences the disulfide exchange kinetics [24]. Since neighboring positive charges can facilitate the disulfide exchange, pLL serves as a more favorable MONA backbone than pAsp. Moreover, polypeptide backbones without PDS groups showed moderated FRET signal after mixing with BSA (Fig. 1D and E), confirming that the binding is primarily mediated by the PDS groups. Also, pre-blocking the thiol groups of BSA with *N*-(2-Aminoethyl)maleimide (NAM) markedly reduced the FRET signal (Supplementary Figure S8), further confirming that the interaction is driven by the reaction between the PDS moieties and BSA thiols.

The binding between BSA and MONA was further analyzed at the single molecule level by quantifying the molecular diffusion rates of BSA + MONA mixtures using fluorescence correlation spectroscopy (FCS) (Supplementary Table S1) [31]. Compared to free MONA samples, the BSA + MONA mixtures exhibited lagged autocorrelation function (ACF) curves (Supplementary Figure S9A) and decreased diffusion coefficients (Fig. 1F), confirming the association of the MONA candidates into larger structures. Particularly, the diffusion coefficient of BSA + $pLL_{25}(PDS)_8$ was comparable to that of standard BSA, indicating efficient conjugation. In contrast, BSA + $pAsp_{25}(PDS)_7$ showed a higher diffusion coefficient, suggesting lower conjugation efficiency that led to the presence of a larger proportion of unbound polymers with high diffusion mobility. To understand the interaction of $pLL_{25}(PDS)_8$ and $pAsp_{25}(PDS)_7$ towards BSA, we conducted molecular dynamics (MD) simulations (Fig. 1G). $pLL_{25}(PDS)_8$ exhibited more efficient association with BSA compared to $pAsp_{25}(PDS)_7$, as evidenced by a higher number of atomic contacts with BSA (Fig. 1H) and smaller solvent accessible surface area (SASA) in the complex (Fig. 1I). These results indicate pLL as a more effective MONA backbone than pAsp.

The polymer backbone length also plays a critical role. BSA + $pLL_{50}(PDS)_{11}$ showed an extremely low diffusion coefficient, indicating the formation of large aggregates with hydrodynamic radius around 16 nm. Furthermore, the single molecular fluorescence intensity (count per molecule) of BSA + $pLL_{50}(PDS)_{11}$ increased compared to free $pLL(PDS)_{50}$ (Supplementary Table S1), indicating that multiple (5.5 on average) polymers associated in a single complex (Supplementary Figure S9B). In contrast, $pLL_{25}(PDS)_8$ conjugated to BSA at a 1:1 stoichiometric ratio, confirming specific binding *via* the single active thiol group of albumin [32]. In summary, by tuning the backbone structure and length, we identified $pLL_{25}(PDS)_8$ as the optimal material for making MONA and used this formulation for the following studies.

The reversibility of the interaction between MONA and BSA was tested in the presence of GSH, an accelerator of disulfide exchange [23]. Addition of GSH into BSA + MONA mixture caused a concentration-dependent decrease of FRET signal (Fig. 1J), indicating the dissociation of the disulfide crosslinking between MONA and BSA. This GSH-facilitated disulfide exchange offers the opportunity for a dynamic switch of the binding target of the polymers. To confirm this, Cy3-labeled BSA was added to a pre-mixed solution of Cy5-labeled MONA and unlabeled BSA (Fig. 1K and L). Over time, the gradual emergence of FRET signals confirmed transfer of MONA to the newly introduced Cy3-labeled BSA. Moreover, inclusion of GSH accelerated this exchange, corroborating its role in promoting disulfide reshuffling between binding chaperones.

2.2. MONA re-localizes to cancer cell membrane via GSH-accelerated disulfide exchange

Considering the elevated levels of reactive thiol groups on the surface of cancer cells [8,14], we hypothesized that MONA could anchor to cancer cell membrane *via* disulfide exchange. This was validated by incubating 4T1 cells with a BSA + MONA mixture at 4 °C, in which fluorescence-labeled MONA polymers accumulated on the cell (Fig. 2A and B). Moreover, MONA highly co-localized with cell membrane structure (Fig. 2C). Even after prolonged (24 h) incubation at 37 °C, a substantial fraction of MONA remained associated with cell membrane (Supplementary Figure S10). We next investigated the underlying mechanism responsible for the interaction between MONA and the cell membrane. Pre-blocking cell surface thiols significantly reduced MONA binding (Supplementary Figure S11), indicating that the reactive thiols are necessary for the binding of MONA. Moreover, the pLL_{25} backbone exhibited negligible cellular binding (Supplementary Figure S12 and Fig. 2D and E). These results confirm the binding capability of MONA is predominantly mediated by disulfide cross-linkages between MONA and cell membrane thiols.

Notably, the presence of GSH in the culture medium significantly accelerated the binding of MONA to cell membrane (Fig. 2A and B and Supplementary Figure S13), suggesting extracellular GSH can accelerate the disulfide exchange to facilitate the transfer of MONA from albumin to cell membrane. On the other hand, the number of PDS groups on MONA significantly influences its interaction with cells. We prepared a formulation bearing only a single PDS group, namely $pLL_{25}(PDS)_1$. This formulation exhibited markedly weaker cell-binding capability compared with MONA (Supplementary Figure S12 and Fig. 2D and E), indicating that the introduction of multiple PDS groups facilitates more stable interactions with the cell surface.

We also noticed that the membrane-binding efficiency of MONA varied across different cell types. For example, higher fluorescence intensity of MONA was found on 4T1 cells than that on 3T3 cells (Fig. 2F). A broader screening revealed MONA has higher binding to cancerous cells (4T1, CT26, Jurkat, B16F10, HT29, and BxPC3 cells) than in non-cancerous cells (DC 2.4, Raw264.7, 3T3 cells, and splenocytes) (Supplementary Figure S14-15). To investigate whether this differential binding was due to variations in surface thiol level, we stained cells with AlexaFluor 488-maleimide to evaluate the abundance of reactive thiol groups on the cells [33]. The analysis confirmed that cancer cells have higher levels of reactive surface thiols than non-cancer cells (Supplementary Figures S16-17), with a strong correlation between thiol abundance and MONA binding efficiency (Fig. 2G). These findings demonstrate that MONA selectively targets cancer cells *via* thiol-mediated membrane anchoring.

2.3. Redox response of MONA balances transcytosis and membrane binding

We then investigated the cellular uptake and intracellular transport of MONA at 37 °C. When applied alone, MONA ound to the cell membrane with minimal internalization (Fig. 3A and B). In contrast, MONA + BSA showed partial binding to cell membrane, and internalization into intracellular space. Moreover, the presence of GSH in the medium increased cell membrane binding and decreased the internalization fraction, suggesting that MONA uses albumin in the internalization process, while disulfide exchange facilitates MONA's binding to cell membrane.

Since albumin can achieve high intratumoral permeability by transcytosis [34–36] we investigated if MONA could take advantage of such mechanism. A transwell assay was conducted to evaluate the rate of MONA to cross a monolayer of cells. Mixing MONA with albumin resulted in the highest transport rate (Fig. 3C). Moreover, the transport efficiency was significantly suppressed by methyl-β-cyclodextrin (MβCD) and by supplementation with excess BSA, whereas it was not

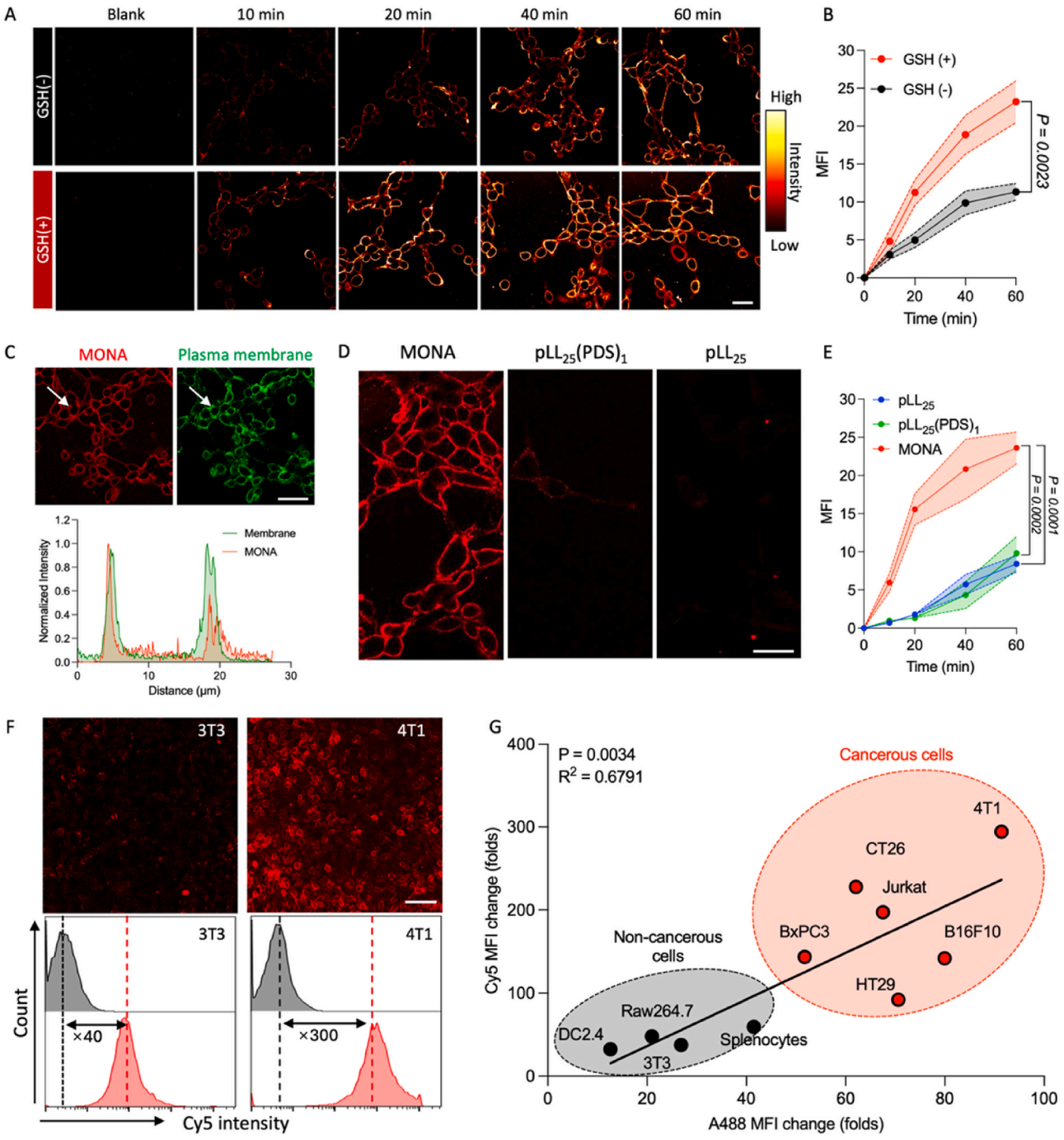

Fig. 2. MONA re-localizes to the cancer cell membrane *via* GSH-accelerated disulfide exchange. A. Representative CLSM images showing the binding of MONA to 4T1 cells in mediums supplemented with or without GSH (1 mM). Scale bar = 25 μm. **B.** Quantified mean fluorescence intensities (MFI) from cells in the images of Fig. 2A. Data were plotted as the mean ± S.D., $n = 5$ images analyzed. The values at 60 min were compared *via* Student's *t*-test. **C.** Representative CLSM images showing the co-localization of MONA with cell membrane after incubating cells with MONA + BSA for 1 h. The cell membrane was stained by CellMask Green staining reagent. Scale bar = 50 μm. The intensity distribution of red and green fluorescence along the direction indicated by the arrow is plotted at the lower panel. **D.** Representative CLSM images showing the binding of MONA, $pLL_{25}(PDS)_{1.5}$ or pLL_{25} to 4T1 cells after 60 min incubation. Scale bar = 25 μm. **E.** Quantified MFI from 4T1 cells after incubating with MONA, $pLL_{25}(PDS)_{1.5}$ or pLL_{25} for different time durations. Data were plotted as the mean ± S.D., $n = 5$ images analyzed. **F.** Representative fluorescence microscope images showing MONA binding to 3T3 (left) and 4T1 (right) cells are shown at the upper panel. Scale bar = 100 μm. Flow cytometry analysis quantifying the fluorescence intensities from 3T3 (left) and 4T1 (right) cells before and after treating with MONA are shown at the lower panel. **G.** Correlation analysis between the MONA binding efficiency and surface reactive thiol level of different cells. The result was evaluated by Pearson correlation analysis. (For interpretation of the references to color in this figure legend, the reader is referred to the Web version of this article.)

significantly inhibited by chlorpromazine or amiloride (Fig. 3D). These results indicate that the transport of the BSA–MONA complex is primarily mediated by albumin-dependent transcytosis. We then evaluated the penetration of MONA in 4T1 cell spheroids. Without presence of albumin, MONA showed clear binding to the surface of the spheroids (Fig. 3E upper panel, Fig. 3F). On the other hand, mixing MONA with BSA lead to a deeper penetration in the spheroids compared to MONA alone (Fig. 3E middle panel, Fig. 3F). Moreover, the addition of MβCD

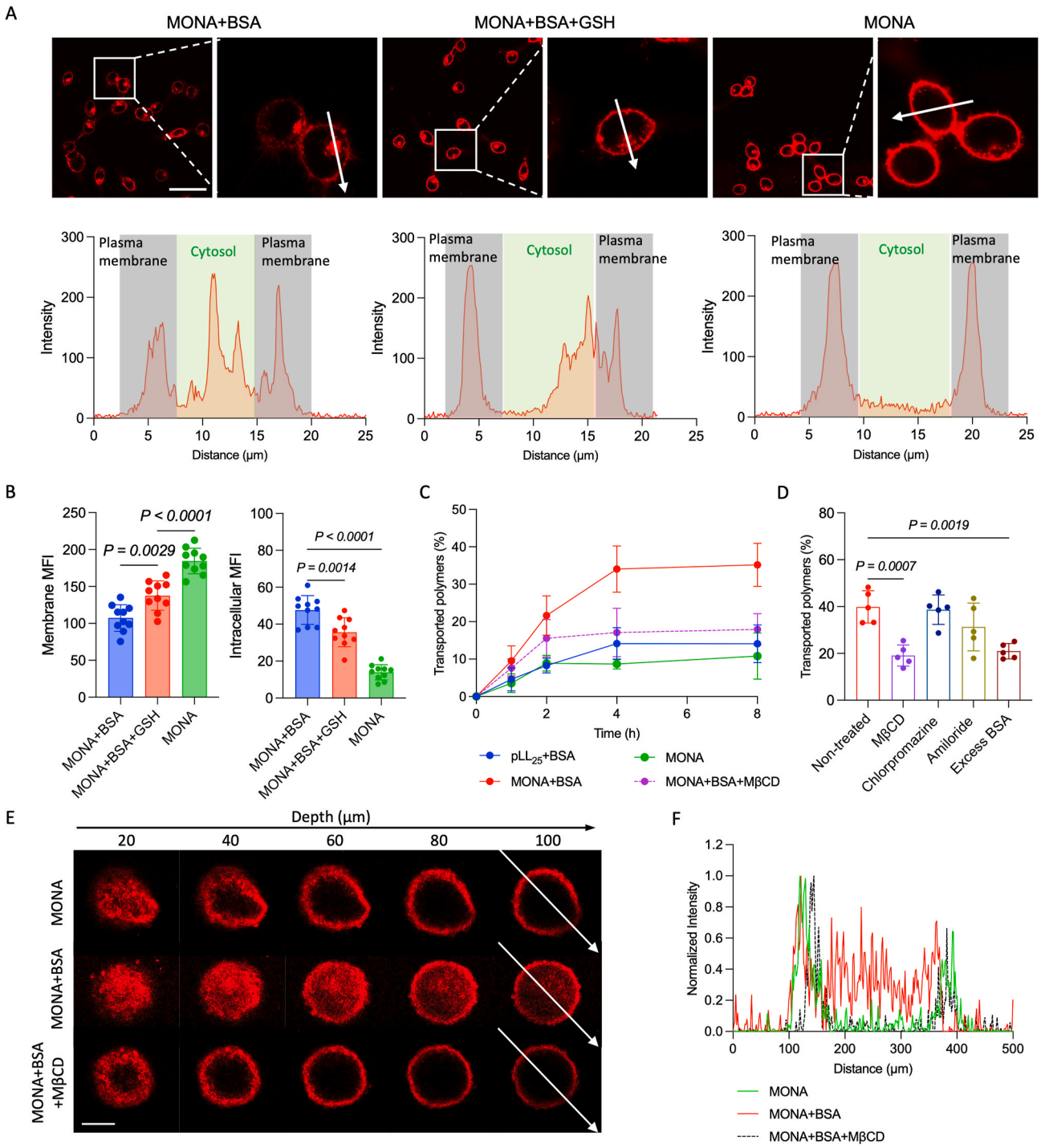

Fig. 3. Redox response of MONA balances transcytosis and membrane binding. A. Representative CLSM images showing the distribution of Cy5-labeled MONA after incubating with 4T1 cells under 37 °C. Scale bar = 50 μm. The fluorescence intensity profiles along the arrows are plotted at the lower panel. **B.** Quantified MFI from cell membrane and intracellular spaces in the images of Fig. 3A. Data were plotted as the mean ± S.D., $n = 10$ cells analyzed. Results were compared *via* one-way ANOVA. **C.** Time-dependent profile of polymer transport across the transwell assay. Data were plotted as the mean ± S.D., $n = 3$ samples. **D.** Transport efficiency of BSA + MONA complex across the transwell assay after 8 h incubation. The cells were pre-treated with MβCD, chlorpromazine, amiloride, or excess BSA. Data were plotted as the mean ± S.D., $n = 4$ samples. Results were compared *via* one-way ANOVA. **E.** Representative CLSM images of 4T1 spheroids after incubating with Cy5-labeled MONA under different conditions. Scale bar = 100 μm. **F.** Plot profile indicating the distribution Cy5 fluorescence intensities along the arrows in Fig. 3E.

inhibited the penetration (Fig. 3E lower panel, Fig. 3F). These results suggest that albumin binding facilitates the transcellular transport of MONA within tumors, thereby increasing the probability of MONA encountering tumor cell membranes and reinforcing its targeting capability.

2.4. Disulfide-mediated albumin hitchhiking controls blood circulation

The association with albumin can enhance the pharmacokinetics of molecules to achieve long circulation in blood [37–39]. Thus, we investigated the pharmacokinetics of MONA in healthy mice. Cy5-labeled MONA was i.v. injected from the tail vein. The circulation

profile of the polymers in the bloodstream was visualized by using intravital confocal laser scanning microscope (IVCLSM) to observe the vessels on the earlobe skin of the mice. pLL_{25} showed only a transient circulation in the blood ($t_{1/2} \approx 7$ min) and caused aggregates at micrometer size (Fig. 4A and B upper panel, Supplementary Video S1). In contrast, MONA exhibited a stable circulation, showing a half-life ($t_{1/2}$) ≈ 80 min in the vessel (Fig. 4A and B middle panel, Supplementary Video S2). Moreover, the pharmacokinetic property of MONA exhibited remarkable sensitivity to the environmental GSH level. Upon i.v. injection of GSH, the circulation profile of MONA immediately shifted, showing rapid clearance from the bloodstream (Fig. 4A and B lower panel, Supplementary Video S3). This finding indicates that the stable circulation of MONA arises from the thiol-mediated hitchhiking with serum albumins.

To further confirm this hitchhiking mechanism underlying this prolonged circulation of MONA, we investigated the interactions between MONA and albumin *in vivo* using FRET-based IVCLSM observation (Fig. 4C). First, Cy3-labeled BSA was i.v. injected to mice to establish a stable circulation of fluorescent-labeled albumins in the bloodstream. After 10 min, Cy5-labeled polymers were i.v. injected. Injection of pLL_{25} failed to induce any detectable FRET signal in the vessels throughout the whole experiment (Fig. 4C and D upper panel, Supplementary Video S4). Injection of the $pAsp_{25}(PDS)_7$ polymer resulted in a weak FRET signal in the bloodstream (Supplementary Figure S18, Supplementary Video S5). In contrast, immediately after injection of MONA, strong FRET signals could be observed in the blood vessels, indicating the binding of MONA to the pre-injected fluorescent BSA (Fig. 4C and D middle panel, **Supplementary** Video S6). Interestingly, a bolus i.v. injection of GSH triggered a rapid decline of the FRET signal in the vessels (Fig. 4C and D lower panel, **Supplementary** Video S7), demonstrating that the dissociation of the BSA-MONA complex was facilitated by GSH. Without the GSH injection, the FRET signal remained stable for several hours (**Supplementary** Video S6). These data confirm the first stage ("Hide") of MONA's working mechanism, in which MONA hitchhikes on endogenous albumin to achieve stealthy systemic circulation.

Supplementary data related to this article can be found online at https://doi.org/10.1016/j.biomaterials.2026.124256

2.5. Albumin shuttles MONA across tumor endothelia for disulfide exchange-driven membrane targeting

We then tested the tumor-targeting capability of MONA. Upon i.v. administration, Cy5-labeled MONA achieved strong fluorescence at the tumor site, as determined by *in vivo* whole-body imaging (Fig. 5A, upper panel). On the other hand, the non-modified polymer backbone pLL_{25} exhibited minimal tumor accumulation (Fig. 5A, lower panel). Notably, the tumor accumulation of MONA reached a plateau at approximately 8 h post-injection (Fig. 5B). At this time point, we collected the organs and tumors to assess biodistribution. While pLL_{25} displayed widespread distribution across major organs, MONA showed highly preferential accumulation in tumor tissue (Fig. 5C and D and Supplementary Figure S19).

To reveal the mechanism behind such tumor-targeting capability, IVCLSM was employed to track the transport of albumin-MONA complexes in the tumor vasculature system. To facilitate real-time visualization, 4T1 tumors were inoculated intradermally (i.d.) into the earlobes of mice (Supplementary Figure S20) [40]. Pre-mixed Cy5-labeled MONA and A488-labeled BSA were i.v. administrated. IVCLSM imaging showed that both MONA and BSA extravasated from the tumor vasculature and accumulated within the tumor tissue with synchronous kinetics (Fig. 5E and **Supplementary** Videos S8–S9). This efficient extravasation and subsequent penetration into the TME can be associated with active transcytosis across the vascular endothelial cells, coupled with the enhanced permeability and retention (EPR) effect of albumin [41–45].

Supplementary data related to this article can be found online at https://doi.org/10.1016/j.biomaterials.2026.124256

To visualize the dynamics of the disulfide exchange inside the tumor, another FRET-based IVCLSM observation was conducted using Cy3-labeled BSA and Cy5-labeled MONA (Fig. 5F and **Supplementary** Video S10). Time-resolved FRET analysis within the tumor revealed a biphasic signal profile. The rapid increase of FRET shortly after injection indicated the tumor accumulation of MONA as a BSA-MONA complex. However, the decline of the FRET signal indicates the dissociation of MONA from BSA within the TME, confirming the occurrence of disulfide exchange process. Upon dissociation, MONA bound directly to the membranes of tumor cells, as confirmed by tissue sections (Fig. 5G–H). These findings validate the "Seek" stage of MONA inside tumors.

Supplementary data related to this article can be found online at https://doi.org/10.1016/j.biomaterials.2026.124256

2.6. Photosensitizer-conjugated MONA induces light-triggered ICD

To evaluate the potential of MONA as a therapeutic platform, the photosensitizer IR783 was selected as a model cargo. IR783 was covalently conjugated to the side chains of $pLL_{25}(PDS)_8$ or pLL_{25} *via* a substitution reaction between the primary amines of the polymer and the meso-chloride group of IR783 [46] (Supplementary Scheme S3 **and** Supplementary Figure S21-23). The resulting photosensitizing polymers, MONA-IR and pLL-IR, exhibited comparable absorption spectra in aqueous buffer, with a maximal absorbance around 630 nm (Supplementary Figure S24). Upon irradiation with a 650 nm laser (0.5 W/cm^2), both polymer solutions demonstrated strong photothermal activity, raising solution temperatures above 45 °C within 5 min (Fig. 6A and B). In addition, both polymers generated reactive oxygen species (ROS) upon light activation, as evidenced by the degradation of 1, 3-diphenylisobenzofuran (DPBF) probe (Fig. 6C).

The cytotoxicity of the polymers was subsequently assessed in 4T1 cells. In the absence of light, both MONA-IR and pLL-IR exhibited minimal toxicity, maintaining cell viability above 80% at concentrations below 10 μM (Supplementary Figure S25). On the other hand, both polymers induced photocytotoxicity under light irradiation. Notably, MONA-IR showed significantly higher light-induced cytotoxicity than pLL-IR (Fig. 6D), which should be due to its effective binding to cell membrane.

Given that membrane-binding photosensitizers have potential for triggering membrane rupture and elicit ICD [30], we investigated the mechanism of the photocytotoxicity of MONA-IR. Clearly, with light irradiation, MONA-IR led to a substantial release of lactate dehydrogenase (LDH) from 4T1 cells (Fig. 6E), indicating plasma membrane disruption [47]. Additionally, we evaluated the exposure of calreticulin (CRT) on the cell surface, which is a hallmark of ICD [48,49]. Compared to untreated cells and those treated with pLL-IR (Fig. 6F upper and middle panel), the cells exposed to MONA-IR under light irradiation exhibited significantly increased CRT level on cell surface (Fig. 6F lower panel), confirming the induction of ICD. As ICD can promote antigen presentation and activate antitumoral immune responses [50]. We next assessed the immunostimulatory potential of treated cells using a transwell co-culture model with DC 2.4 dendritic cells (Fig. 6G). Following treatment with MONA-IR and light irradiation, 4T1 cells stimulated the maturation of DC 2.4 cells, as demonstrated by increased IL-6 secretion (Fig. 6H) and upregulation of CD80 and CD86 (Fig. 6I and J) in DC 2.4 cells. These results suggest that MONA-IR–mediated phototherapy generates immune-stimulatory signals capable of activating immune cells.

2.7. MONA-IR drives effective photoimmunotherapy and systemic tumor control

The therapeutic efficacy of MONA-IR was evaluated in the immunosuppressive 4T1 tumor model. We first evaluated the safety profile of MONA-IR. Healthy mice received i.v. injections of MONA-IR or pLL-IR for three consecutive days (Supplementary Figure S26A). Blood

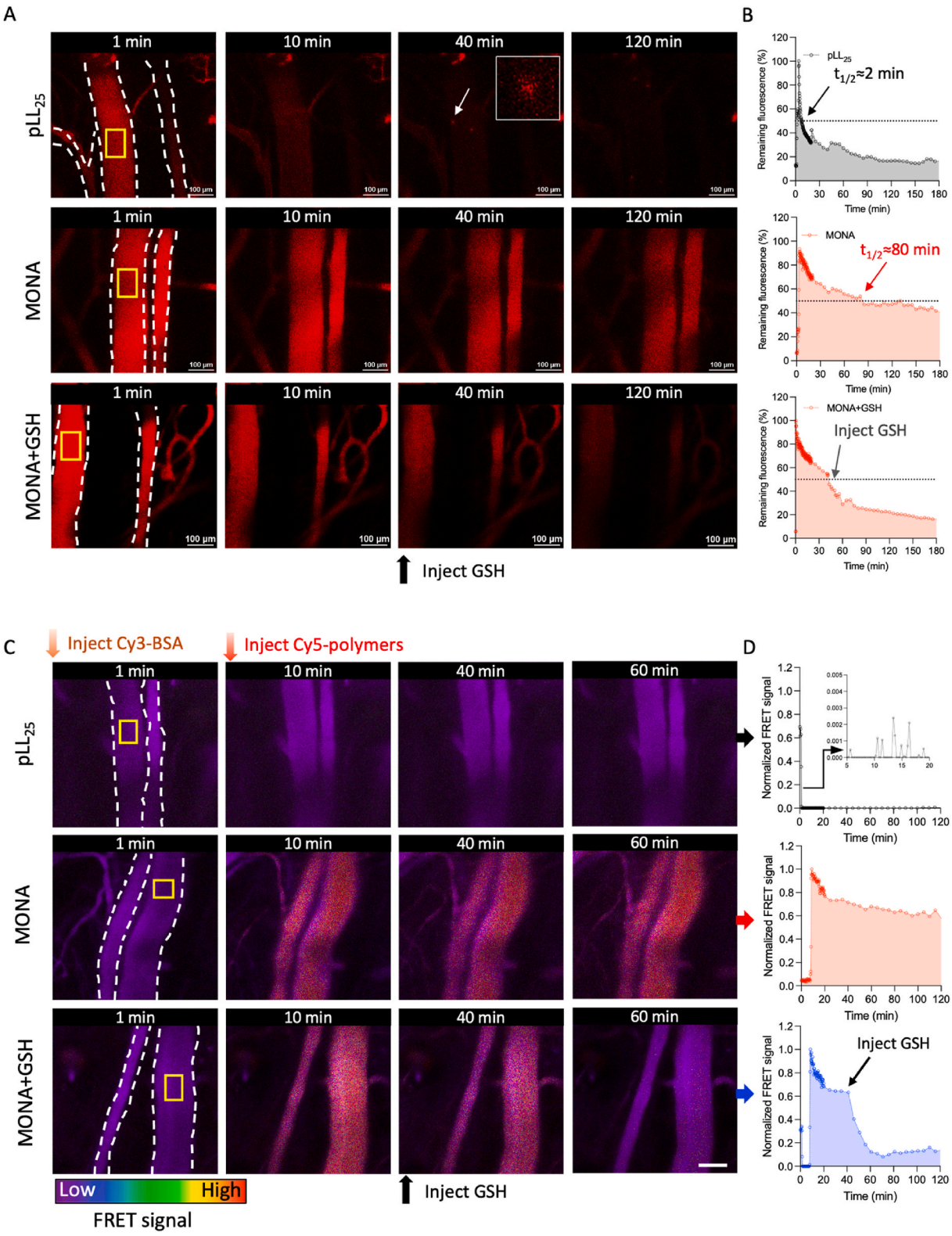

Fig. 4. MONA hitchhikes albumin for stable circulation. A. IVCLSM images of the vessels on mice earlobe after i.v. injection of pLL_{25} and MONA polymers. For MONA-injected mouse, GSH was injected at 40 min. Vessels are marked with the dashed lines. Scale bar = 100 μm. The arrow indicates aggregates in blood stream. **B.** Quantified time-dependent profile of the fluorescence intensities observed from the ROIs (yellow boxes in Fig. 4A) in vessels indicating the blood circulation of the polymers. **C.** Intravital FRET observation evaluating the *in-situ* association of MONA and albumin in blood. Cy3-labeled BSA was i.v. injected at the beginning (0 min). Cy5-labeled polymers (pLL_{25} or MONA) were injected at 10 min. GSH was injected at 40 min. Scale bar = 100 μm. **D.** Quantified FRET signals in the ROIs (yellow boxes in Fig. 4C) in vessels during the experiment process. (For interpretation of the references to color in this figure legend, the reader is referred to the Web version of this article.)

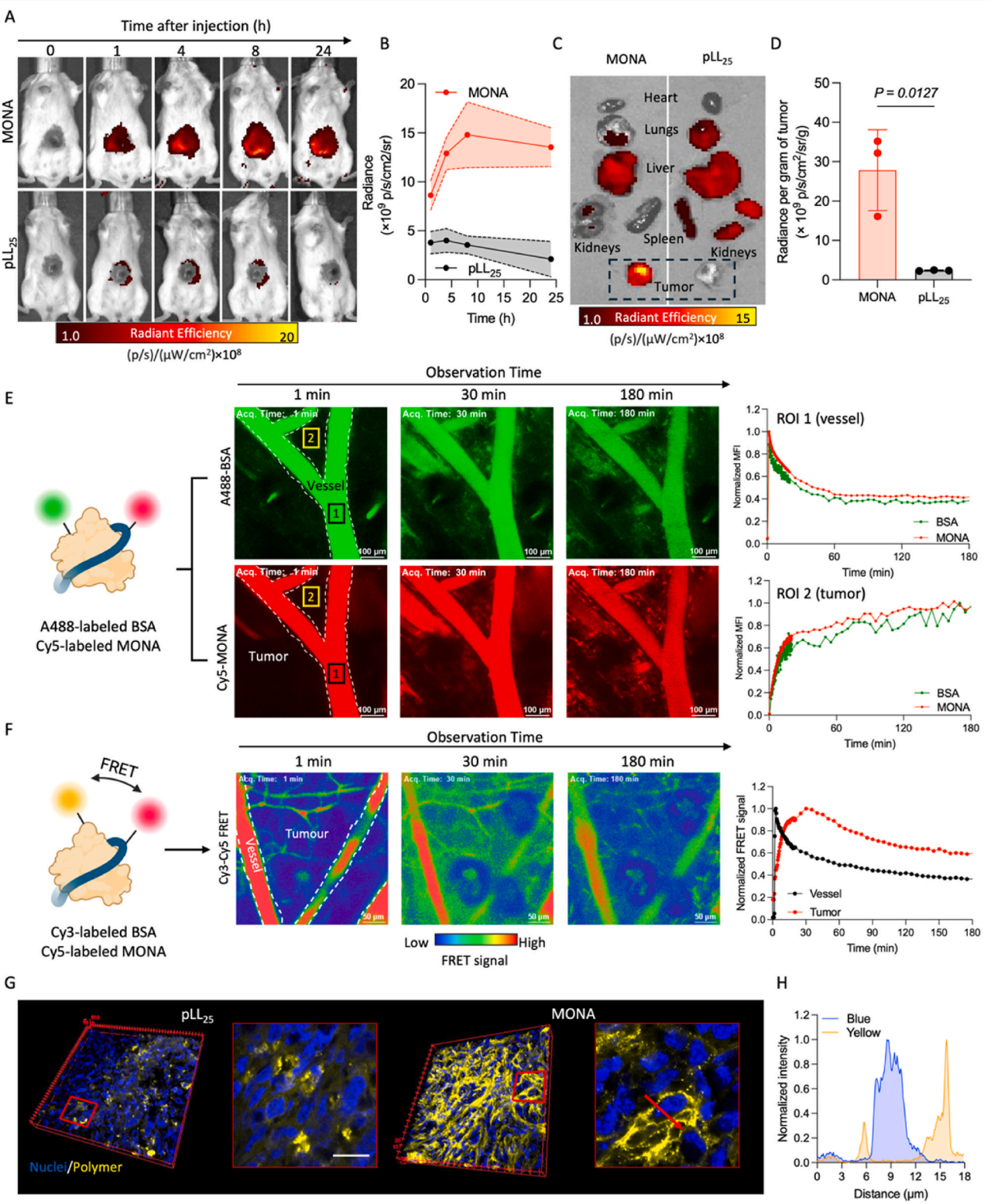

Fig. 5. Albumin shuttles MONA across endothelia for disulfide exchange-driven membrane targeting. A. Representative IVIS image of mice after i.v. injection of Cy5-labeled polymers. **B.** Quantified fluorescence intensities from tumors measured at different time points from the IVIS images in Fig. 5A. Data were plotted as the mean ± S.D., $n = 3$ animals. **C.** Representative IVIS image of excised tissue samples from mice 8 h after i.v. injection of the polymers. **D.** The quantified fluorescence intensities from the excised tumors. Data were plotted as the mean ± S.D., $n = 3$ samples. **E.** IVCLSM observation of 4T1 tumors after i.v. injection of the mixture of A488-labeled BSA and Cy5-labeled MONA. Vessels were marked by white dashed line. ROIs were placed in vessel (ROI 1, black box) and tumor tissue (ROI 2, yellow box) to measure the time-dependent fluorescence profile. Scale bar = 100 μm. **F.** Intravital FRET observation of 4T1 tumors after i.v. injection of the mixture of Cy3-labeled BSA and Cy5-labeled MONA. Vessels were marked by white dashed line. The time-dependent fluorescence profiles in vessel and tumor tissue were measured and plotted at the right panel. Scale bar = 50 μm. **G.** CLSM observation of tumor tissue section slides collected 8 h after i.v. injection of the polymers. Scale bar = 25 μm. **H.** Fluorescence distribution along the direction indicated by the red arrow in Fig. 5G. (For interpretation of the references to color in this figure legend, the reader is referred to the Web version of this article.)

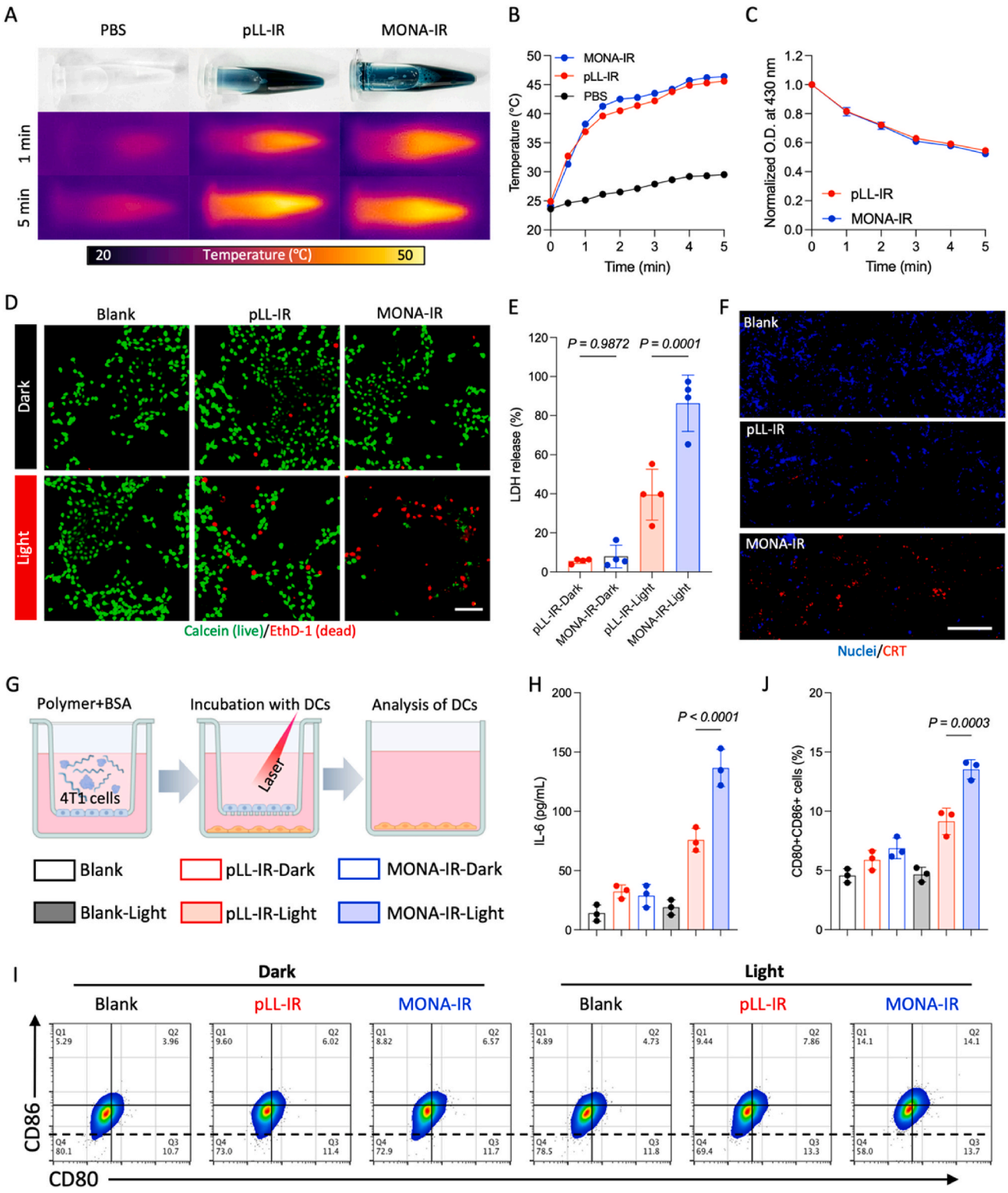

Fig. 6. Photosensitizer-conjugated MONA induces light-triggered ICD. A. Representative thermal photos showing the temperature of the polymer solutions upon light irradiation. **B.** Quantified temperature change of the polymer solutions during continuous irradiation. **C.** Results of DPBF assay measurements evaluating the ROS generation in the polymer solutions under light irradiation. **D.** Representative results of Live/Dead staining on 4T1 cells treated by polymers confirming the light-induced cytotoxic effect. Green: Calcein staining indicating living cells; red: PI staining indicating dead cells. Scale bar = 100 μm. **E.** Fractions of LDH released from the cells after different treatments. Data were plotted as the mean ± S.D., $n = 4$ samples. Results were compared *via* one-way ANOVA. **F.** Representative immunostaining images of 4T1 cells treated by polymers and irradiated by light. CRT exposed on cell surface was stained with red fluorescence. Scale bar = 200 μm. **G.** Schematic illustration of the transwell experiment investigating the interaction between treated 4T1 cells and dendritic cells. 4T1 cells were treated with polymers and light irradiation, then placed to the wells coated with DC 2.4 cells. **H.** IL-6 levels in the medium measured by ELISA. Data were plotted as the mean ± S.D., $n = 3$ samples. Results were compared *via* one-way ANOVA.**I.** Representative flow cytometry scattering plot showing the expression level of CD86 and CD80 on DC 2.4 after different treatments. **J.** Quantified fractions of $CD80^{+}CD86^{+}$ cells in the treated DC 2.4 cells. Data were plotted as the mean ± S.D., $n = 3$ samples. Results were compared *via* one-way ANOVA. (For interpretation of the references to color in this figure legend, the reader is referred to the Web version of this article.)

samples were collected on Day 7 and Day 14 to measure the levels of inflammatory cytokines (IL-1β and IL-6) (Supplementary Figure S26B) and toxicity markers (Supplementary Figure S26C), respectively. The results showed that treatment with either MONA-IR or pLL-IR did not cause a significant increase in inflammatory cytokines or toxicity markers, demonstrating the favorable safety of MONA-IR. We then evaluated the pharmacokinetics of MONA-IR. Clearly, MONA-IR showed similar pharmacokinetics as MONA, with a circulation half-life ($t_{1/2}$) ≈ 80 min upon i.v. injection (**Supplementary** Video S11–12 and Supplementary Figure S27). Also, MONA-IR showed much higher intratumoral accumulation than pLL-IR (Supplementary Figure S28). Thus, after systemic administration, MONA-IR conducted effective photothermal therapy in tumors, in which 5 min light irradiation heated the tumors to around 60 °C (Fig. 7A and B). Such hyperthermia induced damage to the tumor tissues (Fig. 7C) *via* apoptotic/necrotic routes (Supplementary Figure S29), and initiated the ICD process, which was confirmed by the upregulation of CRT in tumor tissues (Fig. 7D and E). As a result, the treatment effectively altered the immune infiltration of the tumor, increasing the population of both $CD3^+$ T cells and CD11c + antigen presenting cells in the TME (Fig. 7F).

Supplementary data related to this article can be found online at https://doi.org/10.1016/j.biomaterials.2026.124256

To further reveal the potency of MONA-IR to induce profound immune activation by photo-induced ICD, a multiple orthotopic tumor model was established by inoculating two 4T1 tumors on the mammary fat pads at both sides of mice abdomen. After i.v. injection of MONA-IR and pLL-IR, only one tumor on each mouse was light irradiated (Fig. 7G). MONA-IR treatment profoundly changed the immune infiltration landscape in the TME, significantly upregulating the population of $CD8^+$ cytotoxic T cells, antigen presenting dendritic cells (DCs), and macrophages in the tumors (Fig. 7H and Supplementary Figure S30-32). Notably, besides the irradiated tumors, the non-irradiated tumors also exhibited improvements of immune infiltration, suggesting the occurrence of abscopal effect [51]. As a result, both irradiated and abscopal tumors on MONA-IR-treated mice exhibited significantly inhibited progression (Fig. 7I), with 4 mice out of 5 showing complete response (CR) (Fig. 7J). Meanwhile, all mice in the different treatment groups showed comparable bodyweight changes (Supplementary Figure S33), suggesting the safety of MONA-IR. Hematologic and histological analysis also showed no significant variations during the treatments (Supplementary Figure S34-35). Finally, we performed immune depletion experiments to investigate the mechanism underlying the therapeutic efficacy of MONA-IR and the induced abscopal effect. The treatment experiment was repeated, but anti-CD8α or anti-CD4 antibodies were administered to selectively deplete $CD8^+$ or $CD4^+$ T cells in mice after treatment. Depletion of either $CD8^+$ or $CD4^+$ T cells attenuated the therapeutic efficacy, with $CD8^+$ T cell depletion exerting a significantly stronger inhibition (Supplementary Figure S36). These findings highlight the essential role of T cells, particularly $CD8^+$ T cells, in MONA-IR–mediated therapy, indicating effective immune activation by MONA-IR. Generally, MONA-IR presents a powerful agent for conducting safe and effective photoimmunotherapy against tumors.

3. Conclusion

In this study, we designed a molecular navigator, *i.e.*, MONA, targeting active thiols on the surface of cancer cells. MONA operates *via* a two-stage "Hide-and-Seek" mechanism. In the "Hide" stage, MONA hitchhikes on endogenous albumin to extend circulation and highly accumulate in tumor tissues. Upon entering the TME, the redox imbalance triggers disulfide exchange, enabling MONA's anchoring on the membrane of cancer cells ("Seek" stage). This precise sequence enabled the delivery of photosensitizers with high spatial selectivity in an immunosuppressive model of TNBC, allowing tumor eradication after a single treatment.

MONA exploits dynamic disulfide bonds, allowing to reconfigure its molecular partners *in vivo*. Because MONA must react rapidly with endogenous albumin to secure prolonged circulation and avoid off-target retention, we enhanced the exchange of PDS groups with albumin using the amines in pLL. Our data revealed that disulfide exchange of MONA with albumin was faster than conventional maleimides [52], enabling rapid albumin hitchhiking in the bloodstream and extending circulation half-life by 40-fold compared to unmodified pLL. Other strategies have attempted to strengthen PDS-albumin interactions by incorporating aliphatic chains that dock into albumin's hydrophobic pockets [53]. However, this approach does not catalyze the reaction of PDS with thiols. Moreover, it requires precise spatial positioning in pockets that are distant from the Cys34 and may be susceptible to competition from endogenous fatty acids, which may result in weak attachment. In contrast, MONA combines electrostatic association with albumin and rapid disulfide exchange at Cys34, offering a more robust strategy for albumin hitchhiking than hydrophobic pocket-based methods [53–55]. Furthermore, since the hitchhiking of MONA with serum albumin is reversible and redox-sensitive, MONA enables an *in situ* controllable "on/off blood circulation". In our IVCLSM observations, the administration of exogenous GSH during the "Hide" phase effectively disrupted the MONA-albumin association, resulting in its rapid clearance from the blood stream. This strategy exemplifies an approach for on-demand modulating the pharmacokinetics of therapeutics. Notably, as a modular system, the performance of MONA can be finely tuned by adjusting its structural parameters. In the present study, we showed that variations in backbone composition, chain length, charge condition, and the number of disulfide-reactive moieties on the MONA scaffold substantially influence its albumin hitchhiking efficiency and *in vivo* disulfide exchange behavior. Future studies may expand the MONA platform by exploring diverse backbone architectures and side-chain modifications, *e.g.*, incorporating tertiary amines or other functionalities that may accelerate disulfide exchange [56], to generate a broader library of MONA candidates. This can enable systematic screening to establish structure–activity relationships and guide the rational optimization of next-generation designs for developing versatile theranostic systems [57–60].

The reversible disulfide exchange also underpins the "Seek" phase of MONA. After reaching the tumor *via* albumin-mediated transcytosis, MONA undergoes a second exchange reaction with the abundant thiols on tumor cell surfaces. Both reversibility and rapid kinetics are essential for this step. Conventional maleimide chemistry, while capable of albumin hitchhiking, forms conjugates with impaired reversibility that are susceptible to hydrolysis, which limits the dynamic capability necessary for the "Seek" phase [24,61]. Other approaches have attempted to engage surface thiols through local administration [14,33,62], though the systemic feasibility has remained uncertain. In contrast, MONA seamlessly transitions from albumin-bound circulation to efficient thiol engagement on tumor cells, achieving precise intratumoral delivery with subcellular resolution. To our knowledge, MONA is the first thiol-mediated tumor-targeting platform with such dynamic precision after systemic administration.

Overall, MONA represents a novel strategy for systemic tumor-targeted delivery by targeting chemical groups. Unlike conventional ligand–mediated targeting approaches, MONA exploits the enriched thiols on tumor cells as a chemical handle, potentially overcoming the heterogeneity of receptor expression and enabling broader applicability across different tumor types [63,64]. In the future, MONA may serve as a versatile scaffold for constructing peptide–drug conjugates (PDCs) or other therapeutics [65,66]. Nevertheless, several foreseeable limitations of MONA should be acknowledged. TME heterogeneity inevitably shapes the performance of any synthetic navigator, and MONA may not be the exception. Because disulfide exchange is redox-sensitive, variations in GSH levels across tumor niches are expected to alter the kinetics of MONA's "Seek" phase [63,64,67]. This context-responsiveness may in fact be leveraged to bias activity toward the most reductive tumor regions, enhancing spatial precision. Similarly, the possibility of MONA

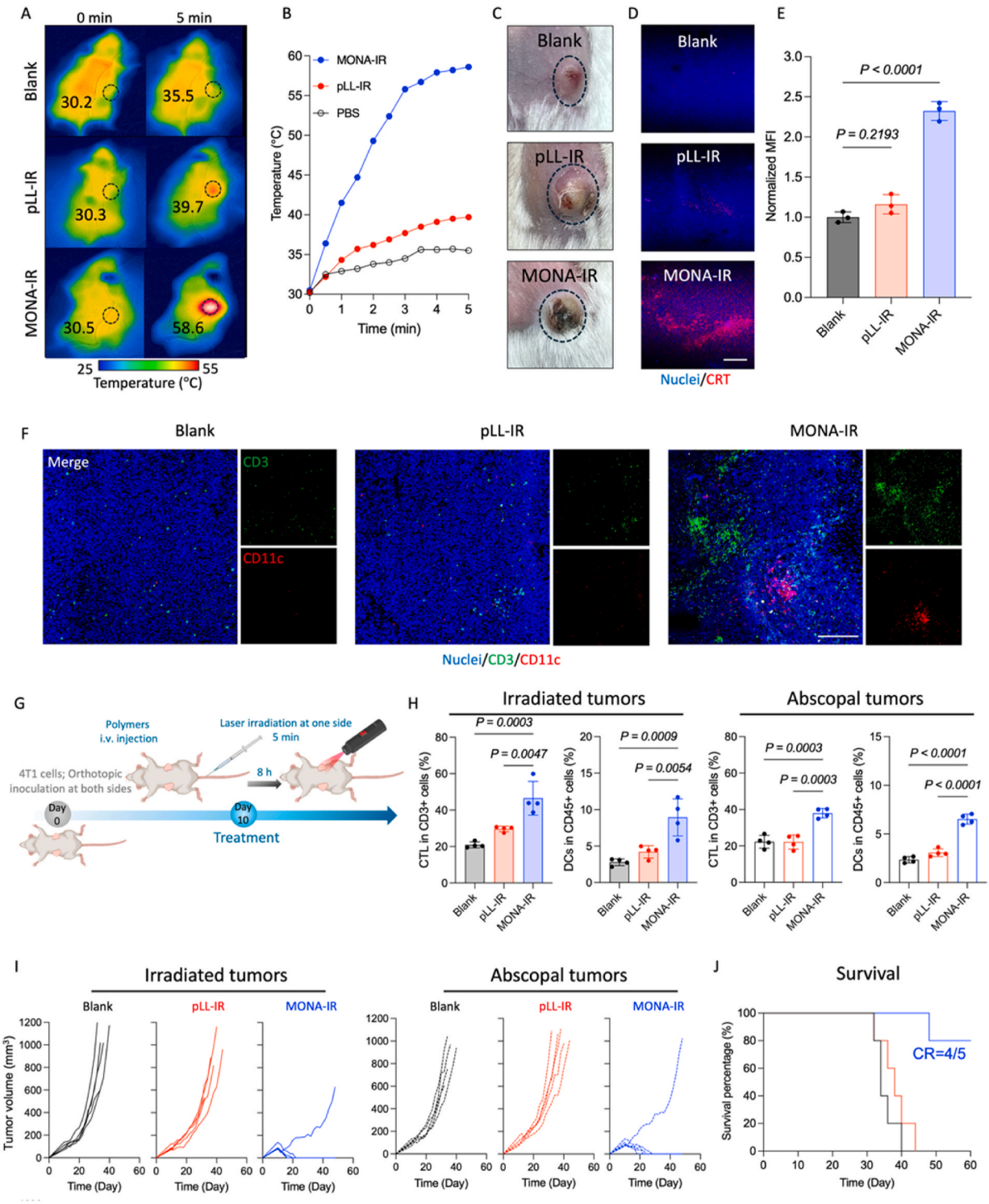

Fig. 7. MONA-IR drives effective photoimmunotherapy and systemic tumor control. A. Representative thermal photos of the mice during light irradiation. The temperature of the tumor area (dashed circle) was measured. **B.** Quantified tumor temperature change during continuous irradiation. **C.** Representative photographs of the tumors 2 days after irradiation. **D.** Representative immunostaining images detecting CRT level in the tumor sections harvested 2 days after irradiation. Scale bar = 100 μm. **E.** Quantified MFI from the images in Fig. 7D indicating the relative level of CRT on tumor cells. Data were plotted as the mean ± S.D., $n = 3$ images. Results were compared *via* one-way ANOVA. **F.** Representative immunostaining images of tumor sections harvested 2 days after irradiation showing the immune infiltration in the tumors. Blue: nuclei; green: CD3; red: CD11c. Scale bar = 100 μm. **G.** Schematic illustration showing the schedule of the experiments to investigate the abscopal effect. **H.** The population of $CD8^+$ CTLs and DCs in the irradiated and non-irradiated abscopal 4T1 tumors after treatment. Data were plotted as the mean ± S.D., $n = 4$ samples. Results were compared *via* one-way ANOVA. **I.** Growth curves of individual tumors during the experiment. **J.** Survival curves of the animals during the experiment. When the tumors exceed 1000 mm^3, the mice were euthanized and counted as dead. Mice survived on Day 90 were determined as complete response. $n = 5$ animals. (For interpretation of the references to color in this figure legend, the reader is referred to the Web version of this article.)

engaging with other redox-dysregulated sites, such as inflamed tissues [68], should be viewed less as a liability than as an opportunity to broaden its scope into inflammation-linked diseases. Beyond oncology, the same design principles could be extended to generate theranostic probes that map redox landscapes *in vivo*, while alternative linkers and payloads will further diversify MONA into a platform for programmable, compartment-specific interventions.

4. Experimental section/methods

4.1. Materials

Benzylamine, *n*-butylamine, 1-(3-dimethylaminopropyl)-3-ethylcarbodiimide (EDC), *N*-hydroxysuccinimide (NHS), dithiothreitol (DTT) and IR783 were purchased from Tokyo Chemical Industry (TCI) (Tokyo, Japan). *N*-trifluoroacetyl-L-lysine *N*-carboxyanhydride (Lys(TFA)-NCA) and *β*-benzyl L-aspartic acid *N*-carboxyanhydride (BLA-NCA) were purchased from ChuoKasei Cooperation (Osaka, Japan). *N*-Succinimidyl 3-(2-pyridyldithio)propionate was purchased from Broadpharm (San Diego, USA). 2-(pyridyldithio)ethylamine HCl was purchased from AmBeed (Arlington Heights, USA). Methyl-β-cyclodextrin (MβCD), chlorpromazine and amiloride were purchased from Sigma-Aldrich (St. Louis, USA). *N,N*-dimethylformamide (DMF), bovine serum albumin (BSA), and glutathione (GSH) were purchased from Fujifilm (Tokyo, Japan). Cyanine3 (Cy3) NHS ester, Cyanine 5 (Cy5) NHS ester and Cy5 maleimide were purchased from Lumiprobe (Cockeysville, USA). AlexaFluor 488 (A488)-NHS ester, A488-malemide, CellMask Green staining dye, mouse IL-6 ELISA kit, mouse IL-1β ELISA kit, Dulbecco's PBS (D-PBS), Dulbecco's Modified Eagle Medium (DMEM) medium, RPMI-1640 (RPMI) medium, Opti-MEM medium, and PerCP/eFluor 710-labeled-anti-mouse CD8α antibody (PerCP/eFluor 710-anti-CD8α) (clone: OX8) were purchased from ThermoFisher (Waltham, USA). Live/Dead staining kit, A647-labeled anti-calreticulin antibody (A647-anti-CRT) (clone: EPR3924), Haematoxylin and eosin (H&E) staining kit, and terminal deoxynucleotidyl transferase dUTP nick end labeling (TUNEL) assay kit were purchased from Abcam (Cambridge, UK). Cell counting kit-8 (CCK-8), LDH assay kit, and Hoechst33342 were purchased from Donjindo (Tokyo, Japan). FITC-labeled-anti-mouse CD3 antibody (FITC-anti-CD3) (clone: 17A2), A647-labeled-anti-mouse CD11c (A647-anti-CD11c) (clone: N418), anti-mouse CD16/32 antibody (anti-CD16/32) (clone: 93), PE-labeled anti-mouse CD11c antibody (PE-anti-CD11c) (clone: N418), FITC-labeled anti-mouse CD80 antibody (FITC-anti-CD80) (clone: 16-10A1), APC-labeled anti-mouse CD86 antibody (APC-anti-CD86) (clone: PO3), PE/Cy7-labeled-anti-mouse CD45 antibody (PE/Cy7-anti-CD45) (clone: I3/2.3), PE-labeled-anti-mouse CD3 antibody (PE-anti-CD3) (clone: 17A2), FITC-labeled-anti-mouse CD4 antibody (FITC-anti-CD4) (clone: GK1.5), PerCP/Cy5.5-labeled-anti-mouse I-A/I-E antibody (PerCP/Cy5.5-anti-MHC-II) (clone: M5/114.15.2), A647-labeled-anti-mouse/human CD11b antibody (A647-anti-CD11b) (clone: M1/70), FITC-labeled-anti-mouse Ly6G antibody (FITC-anti-Ly6G) (clone: 1A8), and PE/Cy5-labeled-anti-mouse CD64 antibody (PE/Cy5-anti-CD64) (clone: X54-5/7.1) were purchased from BioLegend (San Diego, USA). Anti-mouse CD8α (clone: 53-6.7) and anti-mouse CD4 (clone: GK1.5) for immune depletion experiment were purchased from BioXcell (Lebanon, USA).

4.2. Cells and animals

4T1 cells, CT26 cells, Jurkat cells, B16F10 cells, HT29 cells, BxPC3 cells, DC2.4 cells, Raw264.7 cells, 3T3 cells were obtained from Riken BioResource Center (Tsukuba, Japan). 4T1 cells, CT26 cells, Jurkat Cells, B16F10 cells, BxPC3 cells, DC2.4 cells were cultured in DMEM completed with 10% FBS and 1 × penicillin-streptomycin. HT29 cells, Raw264.7 cells and 3T3 cells were cultured in RPMI completed with 10% fetal bovine serum (FBS) (Biosera) and 1 × penicillin-streptomycin (Gibco). Female BALB/c mice were purchased from Charles River Japan (Kanagawa, Japan). The animal experimental procedures were executed according to the Guidelines for Care and Use of Laboratory Animals of The University of Tokyo. Splenocytes were collected from BALB/c mice (female, 9 weeks old) *via* reported method [69,70] and cultured in RPMI medium completed with 10% FBS, 1 × penicillin-streptomycin, 2 mM L-glutamine and 50 μM 2-mercaptoethanol. All cells were kept under 37 °C and 5% CO_2 atmosphere.

4.3. Synthesis and characterization of polymers

The polymers were synthesized following the route described in Supplementary Scheme S1-3. The poly(L-lysine) (pLL) backbone was synthesized *via* a ring opening polymerization (ROP) initiated by benzylamine [71]. Benzylamine (4.5 μL, 41.3 μmol) was mixed with Lys (TFA)-NCA (300 mg, 1.12 mmol; or 600 mg, 2.24 mmol) in 5 mL anhydrous DMF. The mixture was kept stirring under 35 °C for 72 h, followed by precipitation against diethyl ether. The product, poly(L-Lys (TFA)) (pLL(TFA)), was then dissolved in methanol containing 1 M NaOH and kept reacting under 35 °C for 12 h to remove the TFA protection groups. The solution was then dialyzed against water in a dialysis cassette (membrane molecular weight cut-off (MWCO): 1000 Da). The purified solution was lyophilized to get deprotected pLL. The products were obtained in 66% yield for pLL_{25} and 72% yield for pLL_{50}. The polymer was characterized by ^{1}H NMR (DMSO-d_6, 80 °C) and gel permeation chromatography (GPC) (Extrema, JEOL, Japan) (eluent: MeOH/H_2O (v/v = 30%); temperature: 25 °C; flow rate: 0.75 mL min^{-1}; detector: UV/Abs 220 nm).

The pyridyl disulfide-modified pLL (pLL(PDS)) was synthesized by conjugating *N*-succinimidyl 3-(2-pyridyldithio)propionate to the side chain of pLL. For the reaction, pLL (DP25, 80 mg, 25.5 μmol; or DP50, 160 mg, 25.5 μmol) and *N*-succinimidyl 3-(2-pyridyldithio)propionate (150 mg, 425 μmol, or 30 mg, 85 μmol) were dissolved in 2 mL DMF and stirred under 25 °C for 12 h. The mixture was then purified by precipitation against diethyl ether. The products were obtained in 87%, 93% and 91% yield for $pLL_{25}(PDS)_1$, $pLL_{25}(PDS)_8$ and $pLL_{50}(PDS)_{11}$, respectively. The polymer was characterized by ^{1}H NMR (DMSO-d_6, 80 °C) and gel permeation chromatography (GPC) (Extrema, JEOL, Japan) (eluent: MeOH/H_2O (v/v = 30%); temperature: 25 °C; flow rate: 0.75 mL min^{-1}; detector: UV/Abs 220 nm). The number of PDS groups conjugated to the polymer was also determined by a colorimetric method [72]. The polymers (1 mg/mL) were dissolved in D-PBS containing DTT (15 mg/mL). The solutions were incubated at 25 °C for 20 min to induce the reductive cleavage of PDS groups. For the standard curve, free 2-(pyridyldithio)ethylamine was dissolved in D-PBS containing DTT and incubated under the same conditions. The UV absorbance of the samples at 343 nm was measured by a spectrometer (Spark Microplate Reader, Tecan, USA) to quantify the pyridine-2-thione released from the cleavage of PDS groups.

The poly(L-aspartic acid) (pAsp) back bone was synthesized *via* a ROP initiated by *n*-butylamine. *n*-butylamine (4.1 μL, 41.3 μmol) was mixed with BLA-NCA (280 mg, 1.12 mmol) in 5 mL anhydrous DMF. The mixture was kept stirring under 35 °C for 72 h, followed by precipitation against diethyl ether. The product, poly(*β*-benzyl L-aspartic acid) (pBLA), was obtained in 82% yield and characterized by ^{1}H NMR (400 MHz NMR, JEOL, Japan) (DMSO-d_6, 80 °C). Next, the pBLA was dissolved in 1 M NaOH aqueous solution and kept reacting under 25 °C for 1 h. The solution was then dialyzed against water in a dialysis cassette (MWCO: 1000 Da). The purified solution was lyophilized to get deprotected pAsp. The pAsp was obtained in 92% yield and was characterized by ^{1}H NMR (D_2O, 25 °C) and GPC (eluent: MeOH/H_2O (v/v = 30%); temperature: 25 °C; flow rate: 0.75 mL min^{-1}; detector: differential refractometer).

The pyridyl disulfide-modified pAsp (pAsp(PDS)) was synthesized by conjugating 2-(pyridyldithio)ethylamine to the side chain of pAsp. For the reaction, pAsp (75 mg, 25.5 μmol), EDC (20 mg, 100 μmol) and NHS (12 mg, 100 μmol) were dissolved in 2 mL MES buffer (50 mM, pH 6.0)

and stirred under 25 °C for 20 min. Next, 2-(pyridyldithio)ethylamine HCl (95 mg, 425 μmol) was added into the mixture, followed by incubation under 25 °C for 12 h. The mixture was then purified by dialysis against pure water (MWCO: 1000 Da) and lyophilized to collect the final product, pAsp(PDS) in 95% yield. The polymer was characterized by ^{1}H NMR (D_2O, 25 °C) and GPC (eluent: D-PBS; temperature: 25 °C; flow rate: 0.75 mL min^{-1}; detector: differential refractometer).

The photosensitizing polymers were synthesized by conjugating IR783 photosensitizer to the side chain of pLL_{25} or $pLL_{25}(PDS)_8$. pLL_{25} (80 mg, 25.5 μmol) or $pLL_{25}(PDS)_8$ (140 mg, 25.5 μmol) were dissolved in 2 mL DMF. IR783 (190 mg, 255 μmol) and triethylamine (TEA) (50 μL, 340 μmol) were added into the solution. The mixture was kept stirring under 25 °C for 12 h, followed by dialysis against DMF (MWCO: 3500 Da) to remove the unreacted IR783. The polymers (pLL-IR and MONA-IR) were collected by precipitation against diethyl ether in 93% and 89% yields, respectively. The products were characterized by by ^{1}H NMR (DMSO-d_6, 80 °C) and GPC (eluent: MeOH/H_2O (v/v = 30%); temperature: 25 °C; flow rate: 0.75 mL min^{-1}; detector: UV/Abs 600 nm).

4.4. Fluorescence labelling of polymers and proteins

The polymers and proteins were labeled with fluorescence dyes. The labelling was conducted by a condensation reaction between the NHS ester of the dyes and the amines on the polymers or proteins. For the reaction, polymers or proteins (10 mg/mL) were dissolved in 50 mM bicarbonate buffer (pH 8.5). Fluorescence dyes were added to the solution. The mixtures were kept under 37 °C in an orbital shaker for a 15 min reaction. The samples were then purified by gel filtration through a PD-10 column filled with Sephadex G25 resin (Cytiva, USA). The fluorophores used in each sample are specified in the description of the experiments in the following context.

4.5. Interactions between polymers and albumin

The stability of PDS-modified polymers in aqueous buffer was first evaluated. Polymers (100 μM) were dissolved in D-PBS and incubated at 25 °C for 24 h. The UV absorbance of the samples at 343 nm was measured using a spectrometer to quantify the pyridine-2-thione released from the cleavage of PDS groups. As a positive control, polymers (100 μM) were dissolved in D-PBS containing DTT (15 mg/mL) and incubated at 37 °C for 20 min, followed by measurement of the absorbance at 343 nm. The binding between polymers and albumin was confirmed by fluorescence resonance energy transfer (FRET) analysis. For this, BSA was labeled with Cy3, and the polymers were labeled with Cy5. BSA (100 μM) and polymers (100 μM) were mixed in D-PBS (10 mM phosphate and 150 mM NaCl, pH 7.4). Cy5-malemide was also used as a standard control. After incubation under 37 °C for different time, the mixture samples were measured by a fluorescence spectrometer (Spark Microplate Reader, Tecan, USA) with a 550 nm excitation light. The FRET signal intensity was defined as:

$$F = \frac{E_{670}}{E_{570}}$$

F refers to the FRET signal intensity. E_{670} and E_{570} are the fluorescence emission intensity of the sample at 670 nm and 570 nm, respectively. To investigate the role of thiol group in the interaction between polymers and BSA, Cy3-labeled BSA (100 μM) was firstly incubated with NAM (200 μM) in D-PBS under 37 °C for 3 h, then incubated with Cy5-labeled polymers to detect the FRET signal.

The binding of polymers to BSA was also confirmed by fluorescence correlation microscopy (FCS). Cy5-labeled polymers (100 μM) and non-labeled BSA (100 μM) were mixed in D-PBS and incubated under 37 °C for 12 h. The samples were loaded onto an 8-well chambered slide and scanned by a confocal laser scattering microscope (CLSM) (LSM-780, Zeiss, Germany) with 633 nm excitation laser. Free Cy5 dye and Cy5-labeled BSA were also measured as the controls. The autocorrelation function (ACF) curve, diffusion time, and the count per molecule (CPM) of each sample were recorded. The diffusion coefficient of each sample was calculated as:

$$D_{sample} = \frac{D_{cy5} t_{Cy5}}{t_{sample}}$$

D_{sample} and t_{sample} refer to the diffusion coefficient and the measured diffusion time of the sample, respectively. D_{cy5} and t_{cy5} are the diffusion coefficient and measured diffusion time of free Cy5 dye, in which t_{cy5} = 280 μm^2 s^{-1} according to Ref. [73].

The hydrodynamic radius of the MONA + BSA binding products were estimated from their diffusion coefficients *via* Einstein-Stokes equation, as follows:

$$r = \frac{k_B T}{6\pi\eta D_{sample}}$$

D_{sample} is the diffusion coefficient of the sample. K_B is Boltzmann constant. T is the temperature during experiment. η is the viscosity of the buffer.

The association number of polymers in one single complex formed with BSA was calculated by comparing the CPM value of BSA + polymers mixture and free polymers as:

$$A = \frac{CPM_{BSA+MONA}}{CPM_{MONA}}$$

To evaluate the reversibility of the disulfide exchange, different concentrations of GSH (0-10 mM) were added to the prepared BSA + polymers mixture. The samples were incubated under 37 °C. After different incubation durations (0-4 h), the FRET signal intensity of each sample was measured.

The disulfide exchange kinetics were then evaluated with a reconstitution model. Cy5-labeled polymers (100 μM) were mixed with non-labeled BSA (100 μM) in D-PBS and incubated under 37 °C for 12 h Cy3-labeled BSA (100 μM) and GSH (1 mM) were then added into the mixture. The sample was incubated under 37 °C and the FRET signal intensity was measured after different incubation duration (0-4 h).

4.6. Molecular dynamics simulation

Molecular dynamics (MD) simulations were performed using GROMACS 2022.6 to investigate the interactions between albumin and the MONA candidates ($pLL_{25}(PDS)_8$ and $pAsp_{25}(PDS)_7$) over a simulation time of 100 ns.The albumin structure was obtained from the Protein Data Bank (PDB ID: 6M4R)[74]. The structures of the polymers were drawn and optimized by ChemDraw 3D. CHARMM36 force field was applied for all simulations, and the parameters were generated using online tool CGenFF. Each simulation system was built by placing an albumin molecule and either $pLL_{25}(PDS)_8$ or $pAsp_{25}(PDS)_7$ in a cubic simulation box with a side length of 10 nm, ensuring a 1 nm distance from the box edges. The systems were solvated with TIP3P water molecules, and Na^+ ions were added to neutralize the overall charge. The complete MD simulation protocol included compound preparation, ion addition, energy minimization, restrained equilibration of the ligand-protein complex, production MD run, and result analysis. The systems were simulated for 100 ns under conditions of 300 K target temperature and 1 bar target pressure. Trajectory data were analyzed using the trjconv module in GROMACS 2022.6. Energy, temperature, and pressure variations during the equilibration phase were evaluated using the energy module. Root mean square deviation (RMSD) and root mean square fluctuation (RMSF) values were calculated using the rms and rmsf modules, respectively. Radius of gyration (Rg) was computed using the gyrate module. Graphs were generated using DuIvyTools, and trajectory videos were created with PyMOL 2.5.2. Covalent bonds that

involved hydrogen atoms were constrained using the LINCS algorithm [75]. Atomic contact pairs were defined when any pairs of atoms were within a 3.5 Å cutoff or closer.

4.7. Binding of MONA with cells

From the above studies, $pLL_{25}(PDS)_8$ was screened out as the optimal MONA formulation. Thus, in the following context, MONA will be used uniformly to denote $pLL_{25}(PDS)_8$.

The binding of MONA to cell membrane was first confirmed by 4T1 cells. Cy5-labeled pLL_{25}, $pLL_{25}(PDS)_1$ or MONA (100 μM) and non-labeled BSA (100 μM) were mixed in D-PBS and incubated under 37 °C for 12 h. The cells were seeded into 8-well chambered slides (10^4/well) and cultured overnight for adhesion. The culture medium was then replaced with fresh RPMI with or without 1 mM GSH. The BSA + polymer mixture was added into the cell culture medium to make a final concentration of the polymers as 10 μM. Cells were placed in 4 °C for incubation. After different durations (10-60 min), cells were washed by D-PBS and loaded to CLSM (LSM-780, Zeiss, Germany) for fluorescence imaging (Ex 633 nm/Em 660 nm). MONA binding was also confirmed by flow cytometry. The cells were seeded into 6-well plate (10^5/well) and cultured overnight for adhesion. The culture medium was then replaced with fresh RPMI with different concentrations of GSH. The BSA + MONA mixture was added into the cell culture medium to make a final MONA concentration of 10 μM. Cells were placed in 4 °C for 60 min incubation. The cells were then trypsinized and suspended in D-PBS, then loaded to a flow-cytometer (FACSAria, BD Biosciences, USA) to detect the fluorescence signal from APC channel. To confirm the spatial distribution of the polymers, the experiment was repeated under the same condition, but the cell membrane was stained by CellMask dye before adding the BSA + polymer mixture. The images were captured after 1 h incubation by CLSM (Ex 488 and 633 nm/Em 520 and 660 nm). To confirm the role of the surface thiols for the binding of pLL(PDS) on the cells, an inhibition experiment was conducted. The cells were pre-treated with 500 μM N-(2-aminoethyle)maleimide for 30 min and washed by D-PBS. The cells were then incubated with BSA + MONA mixture (10 μM MONA) in 4 °C for 1 h, then imaged by CLSM (Ex 633 nm/Em 660 nm). To evaluate the subcellular distribution of MONA over extended incubation times, Cy5-labeled MONA (10 μM) was added to 4T1 cells seeded in 8-well chambered slides (10^4 cells per well). The cells were incubated at 37 °C for different durations (1-, 4-, 8-, and 24- h). The cells were washed with D-PBS and stained with CellMask dye, then imaged by CLSM (Ex 488 and 633 nm/Em 520 and 660 nm).

4.8. Screening of membrane thiol abundance and MONA binding capability on different cells

The experiments were conducted in different cells including 4T1 cells, CT26 cells, Jurkat Cells, B16F10 cells, HT29 cells, BxPC3 cells, DC2.4 cells, Raw264.7 cells, 3T3 cells, and splenocytes isolated from BALB/c mice. Adhesive cells were treated by 0.25% trypsin and prepared as single cell suspension in D-PBS. Floating cells were washed and re-suspended in D-PBS. The cells were diluted to 10^4/mL in D-PBS and placed in 4 °C. The surface thiol levels of the cells were screened by reported method [8]. Briefly, the cells were incubated with Alexa 488-malemide (10 μg/mL in D-PBS) in 4 °C for 15 min. The cells were loaded into the flow cytometer to detect the fluorescence signal from FITC channel. The polymer binding was quantified with a similar protocol. The cells were incubated with BSA + Cy5-labeled MONA mixture (10 μM MONA) in medium under 4 °C for 60 min, then washed by D-PBS and loaded to flow cytometry to detect the fluorescence signal from APC channel. For both experiments, non-treated cells were measured as the background.

4.9. Transport of BSA-MONA complexes

The cellular uptake and transport of BSA-MONA complex were evaluated in 4T1 cells. Cy5-labeled MONA (100 μM) and non-labeled BSA (100 μM) were mixed in D-PBS and incubated under 37 °C for 12 h. The cells were seeded into 8-well chambered slides (10^4/well) and cultured overnight for adhesion. The culture medium was then replaced with fresh RPMI with or without 1 mM GSH. The BSA + MONA mixture or free MONA was added into the cell culture medium to make a final concentration of MONA as 10 μM. Cells were incubated in 37 °C for 4 h. Cells were then washed by D-PBS and loaded to CLSM (LSM-780, Zeiss, Germany) for fluorescence imaging (Ex 633 nm/Em 660 nm).

The transcytosis efficiency of BSA-MONA complexes was quantitatively evaluated in 4T1 cells with a transwell model. 4T1 cells were seeded into the upper chamber (10^5/well) of a 12-well transwell plate and cultured overnight to form a confluent monolayer. The culture medium on the upper chamber was then replaced with fresh Opti-MEM. Free Cy5-labeled MONA, BSA + Cy5-labeled MONA mixture and BSA + Cy5-labeled pLL_{25} (10 μM polymers) were added into the upper chamber. The cells were incubated under 37 °C. At different time points, the solutions in the lower chamber were sampled and the fluorescence intensity from the samples were measured by a fluorometer (NanoDrop 3300, ThermoFisher, USA) to evaluate the transport kinetics of the polymers from upper chamber to lower chamber. To investigate the transport mechanism, the transwell experiment was repeated with cells pretreated with different endocytosis inhibitors. MβCD (5 mM), chlorpromazine (20 μM), amiloride (2 mM), or excess BSA (100 μM) was added to the upper chamber, and the cells were incubated at 37 °C for 1 h. Subsequently, BSA + Cy5-labeled MONA mixture (10 μM) was added to the upper chamber. After an additional 8 h incubation, the solutions in the lower chamber were sampled and the fluorescence intensities were measured.

The permeability of MONA in compact 4T1 cell spheroid was evaluated first. 4T1 cells (10^3cells in 100 μL medium per well) were seeded in low attachment U-bottom 96-well plate. The cells were incubated for 48 h until the spheroids grew to an average diameter ≈200 μm. The spheroids were then transferred into Opti-MEM medium. Free Cy5-labeled MONA or BSA + Cy5-labeled MONA mixture (10 μM MONA) was added to the spheroids. To inhibit transcytosis, 5 mM MβCD was added into the D-PBS. After 4 h incubation under 37 °C, the spheroids were washed by D-PBS, stained by Hoechst 33,342, and imaged with CLSM (Ex 405, 633 nm/Em 450, 650 nm).

4.10. Blood circulation and in vivo albumin binding of MONA

The behavior of MONA in blood circulation after systemic administration was monitored by intravital confocal laser scanning microscope (IVCLSM) (A1R confocal LSM, Nikon, Japan). To quantify the blood circulation profiles, Cy5-labeled pLL_{25} or MONA (10 μg in 100 μL D-PBS) and GSH (50 mM in 100 μL D-PBS) were i.v. injected into the tail vein of BALB/c mice (6-week-old). The earlobe skin of the mice was observed by IVCLSM for continuous fluorescence imaging (Ex 633 nm/Em 660 nm). ROIs were placed inside the vessels, and the mean fluorescence intensities in the ROIs were plotted against time. Definite intensity values were normalized by the maximal intensity found in each ROI.

To confirm the binding of MONA with albumins during blood circulation, a FRET-based CLSM observation was conducted. Cy3-labeled BSA (100 μg in 100 μL D-PBS) was i.v. injected to into the tail vein of BALB/c mice. Ten minutes after the injection of BSA, Cy5-labeled pLL_{25} or MONA (10 μg in 100 μL D-PBS) was i.v. injected. Forty minutes after the injection of BSA, GSH (50 mM in 100 μL D-PBS) was i.v. injected. During the whole process, the earlobe skin of the mice was observed by IVCLSM *via* FRET observation mode recording spectral images (Ex 555 nm; Em Channel I: 570-600 nm, Em Channel II: 650-700 nm). The results were analyzed by NIS Elements Software (Nikon Corp, Japan) with reported method [70]. Briefly, the spectral images were linearly unmixed

to sperate the two channels, and the FRET signal was defined as:

$$F = \frac{AUC_2}{AUC_1}$$

F is FRET signal. AUC_1 and AUC_2 are the area under the curve of channel I spectrum and channel II spectrum, respectively. ROIs were placed in vessels for measuring the mean FRET signal against time. The FRET signal intensities were normalized to the maximal intensities appearing in each ROI to plot the time-dependent profile.

4.11. Establishment of tumor model

Triple negative breast cancer (TNBC) models were established in BALB/c mice (6-week-old). For IVCLSM observation of the tumors, 4T1 cells (10^6 cells in 30 μL D-PBS) were i.d. injected at the earlobe. For other experiments, 4T1 cells (10^6 cells in 100 μL D-PBS) were orthotopically injected at the mammary fat pad at the lower abdomen. The tumor volume was tracked by a caliper and calculated as:

$$V = \frac{1}{2} \times L \times W^2,$$

where V is tumor volume, L and W are the length and width of the tumor, respectively.

4.12. Tumor-targeted accumulation of MONA

The tumor-targeted transport of MONA was first confirmed by IVCLSM observation. To investigate the kinetic profile of MONA and albumin entering tumor, A488-labeled BSA (10 μg) and Cy5-labeled MONA (10 μg) were mixed in 100 μL D-PBS and incubated under 25 °C for 1 h. The mixture was i.v. injected to mice bearing 4T1 tumors. The tumors were observed by IVCLSM for continuous fluorescence imaging (Ex 488 and 633 nm/Em 520 and 660 nm). ROIs were placed in the vessels and tumor tissues for tracking the fluorescence intensities. To investigate the interaction between MONA and albumin in tumor, Cy3-labeled BSA (10 μg) and Cy5-labeled MONA (10 μg) were mixed in 100 μL D-PBS and incubated under 25 °C for 1 h. The mixture was i.v. injected to mice bearing 4T1 tumors. The tumors were observed by IVCLSM for continuous fluorescence imaging *via* FRET observation mode recording spectral images (Ex 555 nm; Em Channel I: 570-600 nm, Em Channel II: 650-700 nm).

The intratumoral accumulation of MONA was quantified in orthotopic 4T1 tumor model. Cy5-labeled pLL_{25} or MONA (10 μg in 100 μL D-PBS) was i.v. injected into mice bearing 4T1 tumors (average tumor volume ≈ 200 mm^3). The mice were imaged by intravital imaging system (IVIS) (SP-BFM-T1, PerkinElmer, USA) to quantify the fluorescence intensities from the tumor area (Ex 640 nm/Em 680 nm). Eight hours after injection, the mice were sacrificed. Organs and tumors were excised and imaged by IVIS. The tumors were frozen in O.C.T. compound (Sakura Finetek, USA) and sliced to 10 μm thickness by a cryostat (CM3050, Leica, Germany). The slices were mounted in antifade mountant with DAPI (Thermal Fisher, USA) and imaged by CLSM (Ex 405 and 633 nm/Em 450 and 650 nm).

4.13. In vitro therapeutic efficacy

The photosensitizing effects of pLL-IR and MONA-IR were evaluated. The polymers (20 μM) were dissolved in D-PBS. The solutions were irradiated a 650 nm diode semiconductor laser source (CivilLaser, Naku Technology, China) at a power density of 0.5 W/cm^2. The temperature of the samples was tracked by a thermal imaging camera (FLIR ONE Pro, FLIR, USA). To evaluate the photodynamic property, DPBF (20 μM) was added into the LITS samples. Upon irradiation with different time, the absorbance of the samples at 430 nm was measured to indicate ROS generation.

The safety of the polymers was validated in 4T1 cells. The cells were seeded into 96-well plate (10^4/well) and cultured overnight. The polymers were added into the medium at different concentrations and incubated for another 24 h. The cell viability was then tested by CCK-8 assay.

The light-induced cytotoxicity was then evaluated. 4T1 cells were seeded into 96-well plate (10^4/well) and cultured overnight. Polymers were added into the medium (10 μM). After 1 h incubation, cells were washed by D-PBS and irradiated by 650 nm laser (0.5 W/cm^2) for 5 min. The cells were then incubated in fresh medium for another 24 h. To evaluate the cell viability, cells were stained with Live-Dead Cell Staining Kit and imaged by a fluorescence microscope (BZ-X800, Keyence, Japan) with GFP and TRITC filters. The LDH level in the medium was quantified by LDH Assay Kit. To detect the exposure of CRT on the cell surface, the cells were also stained with A647-anti-CRT and Hoechst 33,342, then imaged by a fluorescence microscope with DAPI and Cy5 filters.

The capability of polymer treatment inducing the maturation of APC was evaluated *via* a transwell model. 4T1 cells were seeded into the upper chamber (10^5/well) of a 12-well transwell plate and cultured overnight. DC2.4 cells were seeded into the lower chamber (10^5/well) of another 12-well-transwell plate and cultured overnight. pLL-IR or MONA-IR (100 μM) and BSA (100 μM) were mixed in D-PBS and incubated under 37 °C for 12 h. The culture medium of 4T1 cells was then replaced with fresh RPMI supplemented with 1 mM GSH. The BSA + polymer mixture was added into the cell culture medium to make a final concentration of the polymers as 10 μM. The cells were incubated for another 1 h, then washed by D-PBS and changed into fresh medium. The upper chambers containing treated 4T1 cells were moved into the plate containing DC2.4 cells. The 4T1 cells were then irradiated by 650 nm laser (0.5 W/cm^2) for 5 min. After another 24 h incubation, the supernatant samples were measured by ELISA to quantify the IL-6 concentration. The DC2.4 cells were stained by PE-anti-CD11c, FITC-anti-CD80 and APC-anti-CD86 and measured by a flow cytometry (FACSAria, BD Biosciences, USA) *via* the gating strategy shown in Supplementary Figure S37.

4.14. In vivo safety test

The *in vivo* safety profiles of pLL-IR and MONA-IR were evaluated in healthy mice. pLL-IR or MONA-IR (200 μM in 100 μL D-PBS) was i.v. injected into mice for three consecutive days (Day 1–3). One week after the first administration (Day 7), blood samples were collected from the orbital veins using heparinized capillary tubes and centrifuged (1000 g × 10 min) to isolate plasma. The plasma levels of IL-1β and IL-6 were quantified using ELISA. Two weeks after the first administration (Day 14), blood samples were collected again and plasma was isolated for biochemical analysis using a blood analyzer (DRI-CHEM NX10 N, Fujifilm, Japan) to quantify toxicity markers.

4.15. In vivo therapeutic efficacy

The pharmacokinetics of pLL-IR and MONA-IR were evaluated with the same protocol described above by using A488-labeled polymers. The blood circulation profiles were quantified by IVCLSM. Biodistribution in organs and tumors were evaluated by fluorescence images using IVIS.

The photothermal effect and light-induced immunogenic cell death were evaluated. pLL-IR or MONA-IR (200 μM in 100 μL D-PBS) were i.v. injected into mice bearing orthotopic 4T1 tumor (average tumor volume ≈ 200 mm^3). Eight-hours after injection, the tumor area was irradiated by 650 nm laser (0.5 W/cm^2) for 5 min. The temperature of the tumor area was tracked by thermal imaging camera. After 3 days, the tumors were excised and frozen in O.C.T. compound and sliced to 10 μm thickness by a cryostat. To detect the CRT exposure, the slides were stained with A647-anti-CRT and mounted in antifade mountant with DAPI, then imaged by fluorescence microscope with DAPI and Cy5

filters. To evaluate the intratumoral immune infiltration, the slides were stained with FITC-anti-CD3 and A647-anti-CD11c and mounted in antifade mountant with DAPI, then imaged by CLSM (Ex 405, 488, 633 nm/Em 450, 520, 660 nm). For histology evaluation, the slides were stained with H&E staining kit and TUNEL assay kit, then observed by a microscope (BZ-X800, Keyence, Japan) with brightness field.

The therapeutic efficacy of the polymers was evaluated in orthotopic 4T1 tumor model. Mice were inoculated with two 4T1 tumors at both sides of the lower abdomen. pLL-IR or MONA-IR (200 μM in 100 μL D-PBS) were i.v. injected into mice. After 8 h, one of the tumors in each mouse was irradiated by 650 nm laser (0.5 W/cm^2) for 5 min. Three days after the treatment, some of the mice in each group were sacrificed. The tumors were collected and digested in RPMI medium containing 0.2% collagenase to prepare cell suspension. The single cell suspensions were blocked by anti-CD16/32 and stained by Live/Dead fixable near-IR dead cell staining dye. For evaluating infiltrated T cells, the cell samples were stained PE/Cy7-anti-CD45, PE-anti-CD3, FITC-anti-CD4, and PerCP/eFluor 710-anti-CD8. For evaluating DCs and macrophages, cells were stained by PE/Cy7-anti-CD45, PE-anti-CD11c, PerCP/Cy5.5-anti-MHC-II, A647-anti-CD11b, FITC-anti-Ly6G, and PE/Cy5-anti-CD64. The cells were then loaded to flow cytometer and analyzed *via* the gating strategy shown in Supplementary Figure S38-39. Eight-days after treatment, some of the mice in each group were sacrificed for harvesting the blood and organs. Blood was sampled from the abdominal artery and kept in heparinized tubes, then centrifuged (400g × 5 min) to separate the plasma. The plasma was measured to quantify the toxicity markers. The organs were frozen in in O.C.T. compound and sliced to 10 μm thickness by a cryostat, then stained by H&E staining kit and observed by a microscope with brightness field. The remaining mice in each group were kept for tracking the survival. Mice were euthanized when the tumor volume exceeded 1000 mm^3 and counted as dead. To investigate the therapeutic mechanism of MONA-IR and the underlying basis of the induced abscopal effect, immune depletion experiments were performed. The treatment of MONA-IR in the 4T1 tumor model followed the same protocol described above. However, on Days 10, 12, and 14, mice received intraperitoneal injections of either anti-mouse CD8α or anti-mouse CD4 antibodies (200 μg in 100 μL PBS per injection). The sizes of both irradiated and non-irradiated tumors were continuously monitored throughout the experiment. After the biggest tumor exceeded 1000 mm^3, all the mice were euthanized.

CRediT authorship contribution statement

Pengwen Chen: Writing – original draft, Methodology, Investigation, Formal analysis, Data curation. **Guanghao Hu:** Investigation. **Wenqian Yang:** Investigation. **Yuki Nakashima:** Investigation. **Zhining Xu:** Investigation. **Yiyi Yang:** Investigation. **Soichiro Kondo:** Investigation. **Xiwen Chen:** Investigation. **Sosuke Takasugi:** Investigation. **Ervin Kovács:** Resources. **Katsuhito Fujiu:** Resources. **Horacio Cabral:** Writing – review & editing, Writing – original draft, Funding acquisition, Formal analysis, Data curation, Conceptualization.

Declaration of competing interest

The authors declare the following financial interests/personal relationships which may be considered as potential competing interests: Horacio Cabral reports was provided by The University of Tokyo. Horacio Cabral and Pengwen Chen have patent pending to The University of Tokyo. If there are other authors, they declare that they have no known competing financial interests or personal relationships that could have appeared to influence the work reported in this paper.

Acknowledgements

This work was supported by the Project for Cancer Research and Therapeutic Evolution (P-CREATE) (H.C.) from the Japan Agency for Medical Research and Development (AMED). The study was supported by the GAP Fund from The University of Tokyo (H.C.). The work was also supported by the AMED Seeds A grant (A239; H.C.). The study was partially supported by Grants-in-Aid for Scientific Research A (26H02597 and 23H00546; H.C.), Grants-in-Aid for Exploratory Research (22K19541; H.C.), Grant-in-Aid for JSPS fellows (24KF0198; H.C. and P. C.), the Fund for the Promotion of Joint International Research (Fostering Joint International Research (B), 21KK0197; H.C.) from the Japan Society for the Promotion of Science (JSPS).

The authors acknowledge the use of ChatGPT (OpenAI) in copy editing the article, including grammar correction and improving readability. The authors also acknowledge the use of BioRender.com (BioRender) and Cici AI (ByteDance) for creating graphical elements in the schemes.

Appendix A. Supplementary data

Supplementary data to this article can be found online at https://doi.org/10.1016/j.biomaterials.2026.124256.

Data availability

Data will be made available on request.

References

[1] N.N. Pavlova, J. Zhu, C.B. Thompson, The hallmarks of cancer metabolism: still emerging, Cell Metab. 34 (2022) 355–377.
[2] R.M. Robinson, L. Reyes, R.M. Duncan, H. Bian, A.B. Reitz, Y. Manevich, J. J. McClure, M.M. Champion, C.J. Chou, M.E. Sharik, M. Chesi, P.L. Bergsagel, N. G. Dolloff, Inhibitors of the protein disulfide isomerase family for the treatment of multiple myeloma, Leukemia 33 (2018) 1011–1022.
[3] T.F. Kuo, T.Y. Chen, S.T. Jiang, K.W. Chen, Y.M. Chiang, Y.J. Hsu, Y.J. Liu, H. M. Chen, K.K. Yokoyama, K.C. Tsai, H.H. Yeh, Y.R. Chen, M.T. Yang, C.Y. Yang, W. C. Yang, Protein disulfide isomerase a4 acts as a novel regulator of cancer growth through the procaspase pathway, Oncogene 36 (2017) 5484–5496.
[4] E.S.J. Arnér, A. Holmgren, The thioredoxin system in cancer, Semin. Cancer Biol. 16 (2006) 420–426.
[5] Michael Gronow, The cancer cell thiolome – is it time for A Re-Evaluation of its therapeutic potential? Cancer Sci. Res. 7 (2024) 1–8.
[6] W.W. Huber, W. Parzefall, Thiols and the chemoprevention of cancer, Curr. Opin. Pharmacol. 7 (2007) 404–409.
[7] M. Popielarski, H. Ponamarczuk, M. Stasiak, C. Watała, M. Świątkowska, Modifications of disulfide bonds in breast cancer cell migration and invasiveness, Am. J. Cancer Res. 9 (2019) 1554.
[8] F. Goerdeler, E.E. Reuber, J. Lühle, S. Leichnitz, A. Freitag, R. Nedielkov, R. Groza, H. Ewers, H.M. Möller, P.H. Seeberger, O. Moscovitz, Thiol-mediated uptake of a cysteine-containing nanobody for anticancer drug delivery, ACS Cent. Sci. 9 (2023) 1111–1118.
[9] I. Lorenzen, J.A. Eble, E.M. Hanschmann, Thiol switches in membrane proteins - extracellular redox regulation in cell biology, Biol. Chem. 402 (2021) 253–269.
[10] J. Skalska, P.S. Brookes, S.M. Nadtochy, S. Hilchey, C.T. Jordan, M.L. Guzman, S. Maggirwar, M.M. Briehl, S.H. Bernstein, Modulation of cell surface protein free thiols; A potential novel mechanism of action of the sesquiterpene lactone parthenolide in non-hodgkin's lymphoma, Blood 114 (2009) 3774, 3774.
[11] J. Chiu, I.W. Dawes, Redox control of cell proliferation, Trends Cell Biol. 22 (2012) 592–601.
[12] T. Li, S. Takeoka, Enhanced cellular uptake of maleimide-modified liposomes via thiol-mediated transport, Int. J. Nanomed. 9 (2014) 2849–2861.
[13] G. Gasparini, G. Sargsyan, E.K. Bang, N. Sakai, S. Matile, Ring tension applied to thiol-mediated cellular uptake, Angew. Chem. Int. Ed. 54 (2015) 7328–7331.
[14] A.J. Slezak, A. Mansurov, M.M. Raczy, K. Chang, A.T. Alpar, A.L. Lauterbach, R. P. Wallace, R.K. Weathered, J.E.G. Medellin, C. Battistella, L.T. Gray, T. M. Marchell, S. Gomes, M.A. Swartz, J.A. Hubbell, Tumor cell-surface binding of immune stimulating polymeric glyco-adjuvant via cysteine-reactive pyridyl disulfide promotes antitumor immunity, ACS Cent. Sci. 8 (2022) 1435–1446.
[15] M. Brioschi, E. Gianazza, A. Mallia, B. Zoanni, A. Altomare, A.M. Fernandez, P. Agostoni, G. Aldini, C. Banfi, S-Thiolation targets albumin in heart failure, Antioxidants 9 (2020) 763.
[16] G. Colombo, M. Clerici, D. Giustarini, R. Rossi, A. Milzani, I. Dalle-Donne, Redox albuminomics: oxidized albumin in human diseases, Antioxid. Redox Signal. 17 (2012) 1515–1527.
[17] A. Bocedi, G. Cattani, L. Stella, R. Massoud, G. Ricci, Thiol disulfide exchange reactions in human serum albumin: the apparent paradox of the redox transitions of Cys34, FEBS J. 285 (2018) 3225–3237.
[18] P. Famta, S. Shah, N. Jain, D.A. Srinivasarao, A. Murthy, T. Ahmed, G. Vambhurkar, S. Shahrukh, S.B. Singh, S. Srivastava, Albumin-hitchhiking:

fostering the pharmacokinetics and anticancer therapeutics, J. Contr. Release 353 (2023) 166–185.
[19] Y. Yuan, X. Wang, B. Mei, D. Zhang, A. Tang, L. An, X. He, J. Jiang, G. Liang, Labeling thiols on proteins, living cells and tissues with enhanced emission induced by FRET, Sci. Rep. 3 (2013) 3523.
[20] H.B. Pang, G.B. Braun, Z.G. She, V.R. Kotamraju, K.N. Sugahara, T. Teesalu, E. Ruoslahti, A free cysteine prolongs the half-life of a homing peptide and improves its tumor-penetrating activity, J. Contr. Release 175 (2014) 48–53.
[21] T. Yang, Y. Mochida, X. Liu, H. Zhou, J. Xie, Y. Anraku, H. Kinoh, H. Cabral, K. Kataoka, Conjugation of glucosylated polymer chains to checkpoint blockade antibodies augments their efficacy and specificity for glioblastoma, Nat. Biomed. Eng. 5 (2021) 1274–1287.
[22] A.D. Baldwin, K.L. Kiick, Tunable degradation of maleimide-thiol adducts in reducing environments, Bioconjug. Chem. 22 (2011) 1946.
[23] M. Okumura, M. Saiki, H. Yamaguchi, Y. Hidaka, Acceleration of disulfide-coupled protein folding using glutathione derivatives, FEBS J. 278 (2011) 1137–1144.
[24] G.H. Snyder, M.J. Cennerazzo, A.J. Karalis, D. Field, Electrostatic influence of local cysteine environments on disulfide exchange kinetics, Biochemistry 20 (1981) 6509–6519.
[25] S.P. Trimble, D. Marquardt, D.C. Anderson, Use of designed peptide linkers and recombinant hemoglobin mutants for drug delivery: in vitro release of an angiotensin II analog and kinetic modeling of delivery, Bioconjug. Chem. 8 (1997) 416–423.
[26] Y. Tang, H.K. Bisoyi, X.M. Chen, Z. Liu, X. Chen, S. Zhang, Q. Li, Pyroptosis-mediated synergistic photodynamic and photothermal immunotherapy enabled by a tumor-membrane-targeted photosensitive dimer, Adv. Mater. 35 (2023) 2300232.
[27] P. Lu, X. Liu, X. Chu, F. Wang, J.H. Jiang, Membrane-tethered activation design of a photosensitizer boosts systemic antitumor immunity via pyroptosis, Chem. Sci. 14 (2023) 2562–2571.
[28] P. Chen, J. Rong, K. Chen, T. Huang, Q. Shen, P. Sun, W. Tang, Q. Fan, Photo-amplified plasma membrane rupture by membrane-anchoring NIR-II small molecule design for improved cancer photoimmunotherapy, Angew. Chem. Int. Ed. 64 (2025) e202418081.
[29] P.L. Chen, P.Y. Huang, J.Y. Chen, Q.Y. Shi, Y.Y. Zhu, Y. Chen, L.H. Liu, X.Z. Zhang, A self-delivery chimeric peptide for high efficient cell membrane-targeting low-temperature photothermal/photodynamic combinational therapy and metastasis suppression of tumor, Biomaterials 286 (2022) 121593.
[30] X. Wu, J.J. Hu, J. Yoon, Cell membrane as A promising therapeutic target: from materials design to biomedical applications, Angew. Chem. Int. Ed. 63 (2024) e202400249.
[31] J. Langowski, Protein–protein interactions determined by fluorescence correlation spectroscopy, Methods Cell Biol. 85 (2008) 471–484.
[32] Q. Luo, Y. Tao, W. Sheng, J. Lu, H. Wang, Dinitroimidazoles as bifunctional bioconjugation reagents for protein functionalization and peptide macrocyclization, Nat. Commun. 10 (2019) 142.
[33] F. Goerdeler, E.E. Reuber, J. Lühle, S. Leichnitz, A. Freitag, R. Nedielkov, R. Groza, H. Ewers, H.M. Möller, P.H. Seeberger, O. Moscovitz, Thiol-Mediated Uptake of a Cysteine-Containing Nanobody for Anticancer Drug Delivery, ACS Cent Sci 9 (2023) 1111–1118.
[34] Q. Ji, H. Zhu, Y. Qin, R. Zhang, L. Wang, E. Zhang, X. Zhou, R. Meng, GP60 and SPARC as albumin receptors: key targeted sites for the delivery of antitumor drugs, Front. Pharmacol. 15 (2024) 1329636.
[35] B. Zheng, Y. Chen, L. Niu, X. Zhang, Y. Yang, S. Wang, W. Chen, Z. Cai, W. Huang, W. Huang, Modulating the tumoral SPARC content to enhance albumin-based drug delivery for cancer therapy, J. Contr. Release 366 (2024) 596–610.
[36] A. Chlenski, M. Dobratic, H.R. Salwen, M. Applebaum, L.J. Guerrero, R. Miller, G. DeWane, E. Solomaha, J.D. Marks, S.L. Cohn, A. Chlenski, M. Dobratic, H. R. Salwen, M. Applebaum, L.J. Guerrero, R. Miller, G. DeWane, E. Solomaha, J. D. Marks, S.L. Cohn, Secreted protein acidic and rich in cysteine (SPARC) induces lipotoxicity in neuroblastoma by regulating transport of albumin complexed with fatty acids, Oncotarget 7 (2016) 77696–77706.
[37] M.S. Dennis, M. Zhang, Y. Gloria Meng, M. Kadkhodayan, D. Kirchhofer, D. Combs, L.A. Damico, Albumin binding as a general strategy for improving the pharmacokinetics of proteins, J. Biol. Chem. 277 (2002) 35035–35043.
[38] B.R. Kimmel, K. Arora, N.C. Chada, V. Bharti, A.J. Kwiatkowski, J.E. Finkelstein, A. Hanna, E.N. Arner, T.L. Sheehy, L.E. Pastora, J. Yang, H.M. Pagendarm, P. T. Stone, E. Hargrove-Wiley, B.C. Taylor, L.A. Hubert, B.M. Fingleton, K.N. Gibson-Corley, J.C. May, J.A. McLean, J.C. Rathmell, A. Richmond, W.K. Rathmell, J. M. Balko, J.T. Wilson, Potentiating cancer immunotherapies with modular albumin-hitchhiking nanobody–STING agonist conjugates, Nat. Biomed. Eng. 9 (2025) 1719–1739.
[39] W. Song, W. Wei, X. Lan, W. Cai, Albumin binding improves nanobody pharmacokinetics for dual-modality PET/NIRF imaging of CEACAM5 in colorectal cancer models, Eur. J. Nucl. Med. Mol. Imag. 50 (2023) 2591–2594.
[40] D.T. Nguyen, M.J. Baek, S.M. Lee, D. Kim, S.Y. Yoo, J.Y. Lee, D.D. Kim, Photobleaching-mediated charge-convertible cyclodextrin nanoparticles achieve deep tumour penetration for rectal cancer theranostics, Nat. Nanotechnol. 19 (2024) 1723–1734.
[41] E.N. Hoogenboezem, S.S. Patel, J.H. Lo, A.B. Cavnar, L.M. Babb, N. Francini, E. F. Gbur, P. Patil, J.M. Colazo, D.L. Michell, V.M. Sanchez, J.T. McCune, J. Ma, C. R. DeJulius, L.H. Lee, J.C. Rosch, R.M. Allen, L.D. Stokes, J.L. Hill, K.C. Vickers, R. S. Cook, C.L. Duvall, Structural optimization of siRNA conjugates for albumin binding achieves effective MCL1-directed cancer therapy, Nat. Commun. 15 (2024) 1581.
[42] G. Wei, S. Zhang, S. Yu, W. Lu, Intravital microscopy reveals endothelial transcytosis contributing to significant tumor accumulation of Albumin nanoparticles, Pharmaceutics 15 (2023) 519.
[43] J. Mayr, P. Heffeter, D. Groza, L. Galvez, G. Koellensperger, A. Roller, B. Alte, M. Haider, W. Berger, C.R. Kowol, B.K. Keppler, An albumin-based tumor-targeted oxaliplatin prodrug with distinctly improved anticancer activity in vivo, Chem. Sci. 8 (2017) 2241–2250.
[44] Y. Matsumura, H. Maeda, A new concept for macromolecular therapeutics in cancer chemotherapy: mechanism of tumoritropic accumulation of proteins and the antitumor agent smancs, Cancer Res. 46 (1986) 6387–6392.
[45] H. Iqbal, T. Yang, T. Li, M. Zhang, H. Ke, D. Ding, Y. Deng, H. Chen, Serum protein-based nanoparticles for cancer diagnosis and treatment, J. Contr. Release 329 (2021) 997–1022.
[46] P. Chen, S. Li, Z. Xu, H. Cabral, Nanoassemblies of heptamethine cyanine dye-initiated poly(amino acid) enhance ROS generation for effective antitumour phototherapy, Nanoscale Horiz. 9 (2024) 731–741.
[47] B.S. Cummings, R.G. Schnellmann, Measurement of cell death in mammalian cells, Curr. Protoc. 1 (2021) e210.
[48] J. Fucikova, O. Kepp, L. Kasikova, G. Petroni, T. Yamazaki, P. Liu, L. Zhao, R. Spisek, G. Kroemer, L. Galluzzi, Detection of immunogenic cell death and its relevance for cancer therapy, Cell Death Dis. 11 (2020) 1013.
[49] P. Chen, G. Hu, Y. Nakashima, Z. Xu, T. Watanabe, S. Kondo, E. Kovács, H. Cabral, Optoregulated mRNA delivery controls pleiotropic immune signaling for tumor-targeted therapy, Angew. Chem. Int. Ed. 2025 (2025) e202513610.
[50] B. Decraene, Y. Yang, F. De Smet, A.D. Garg, P. Agostinis, S. De Vleeschouwer, Immunogenic cell death and its therapeutic or prognostic potential in high-grade glioma, Gene Immun. 23 (2022) 1–11.
[51] V.G. Collins, D. Hutton, K. Hossain-Ibrahim, J. Joseph, S. Banerjee, The abscopal effects of sonodynamic therapy in cancer, Br. J. Cancer 132 (2024) 409–420.
[52] L. Feng, J. Fang, X. Zeng, H. Liu, J. Zhang, L. Huang, Z. Guo, R. Zhuang, X. Zhang, 68Ga-Labeled maleimide for blood pool and lymph PET imaging through covalent bonding to serum albumin in vivo, ACS Omega 7 (2022) 28597–28604.
[53] S. Qi, Z. Liu, K. Suyama, Y. Tsuchiya, J. Canarejo, K.Q. Phan, N. Yutsudo, A. Shimada, T. Hirota, I. Ieiri, A. Kishimura, T. Muraoka, T. Nose, T. Mori, Y. Katayama, Ligand design with accelerated disulfide formation with serum albumin to extend blood retention, ACS Med. Chem. Lett. 16 (2025) 144–148.
[54] S.H. Zhuo, X. Chen, L. Zhao, T.Y. Wang, J.Y. Su, T. Yang, L. Yang, F. Dong, Y. F. Zhao, Y.M. Li, AlbiCDN: albumin-binding amphiphilic STING agonists augment the immune activity for cancer immunotherapy, RSC Med. Chem. 16 (2025) 1797–1807.
[55] B. Hu, S. Kong, Y. Weng, D. Zhao, A. Hussain, Q. Jiao, S. Zhan, L. Qiu, J. Lin, M. Xie, B. Li, Y. Huang, Lipid-conjugated siRNA hitchhikes endogenous albumin for tumor immunotherapy, Chin. Chem. Lett. 34 (2023) 108210.
[56] K. Yamawake, M. Hayashi, The role of tertiary amines as internal catalysts for disulfide exchange in covalent adaptable networks, Polym. Chem. 14 (2023) 680–686.
[57] S. Đor, Deviécdeviéc, M. Medel, J. Hillaert, E. Masiá, I. Conejos-Sánchez, M. J. Vicent, S. Đor, M. Medel, J. Hillaert, E. Masiá, I. Conejos-Sánchez, M.J. Vicent, Critical design strategies supporting optimized drug release from polymer–drug conjugates, Small 20 (2024) 2303157.
[58] C. Fante, M.J. Vicent, F. Greco, Polymer-Drug Conjugates, Fundamentals of Pharmaceutical Nanoscience, 2024, pp. 109–137.
[59] B. Louage, D. Defreyne, H. Lauwers, J. De Baere, A. Uvyn, H. Peng, Y. Chen, B. G. De Geest, Lysosomal trafficking and degradation of extracellular proteins via multivalent small molecule ligand display on dextran scaffolds, Biomacromolecules 26 (2024) 738–750.
[60] E. Buijs, Z. Nagorna, J.F.R. Van Guyse, M. Barz, Synthesis of heterotelechelic poly (N-ethylglycine) polymers: from polypeptoid lipid conjugates to protein-polymer conjugates, Macromol. Rapid Commun. (2025) e00422.
[61] S.D. Fontaine, R. Reid, L. Robinson, G.W. Ashley, D.V. Santi, Long-term stabilization of maleimide-thiol conjugates, Bioconjug. Chem. 26 (2015) 145–152.
[62] Z. Lian, L. Zheng, S. Liu, J. Zhang, J. Zhou, J. Wu, S. Ouyang, J. Li, H. Yang, Breaking endosomal barriers: thiol-mediated uptake lipid nanoparticles for efficient mRNA vaccine delivery, J. Am. Chem. Soc. 147 (2025) 31530–31540.
[63] R. Ge, Z. Wang, L. Cheng, Tumor microenvironment heterogeneity an important mediator of prostate cancer progression and therapeutic resistance, npj Precis. Oncol. 6 (2022) 31.
[64] M.R. Junttila, F.J. De Sauvage, Influence of tumour micro-environment heterogeneity on therapeutic response, Nature 501 (2013) 346–354.
[65] D. Fan, Y. Cao, M. Cao, Y. Wang, Y. Cao, T. Gong, Nanomedicine in cancer therapy, Signal Transduct. Targeted Ther. 8 (2023) 293.
[66] B.M. Cooper, J. Iegre, D.H. O'Donovan, M. Ölwegård Halvarsson, D.R. Spring, Peptides as a platform for targeted therapeutics for cancer: peptide–drug conjugates (PDCs), Chem. Soc. Rev. 50 (2021) 1480–1494.
[67] C. Jinqiang Wang, X. Sun, W. Mao, W. Sun, J. Tang, M. Sui, Y. Shen, Z. Gu, J. Q. Wang, X.R. Sun, W.W. Mao, J.B. Tang, M.H. Sui, Y.Q. Shen, W.L. Sun, Z.W. Gu, Tumor redox heterogeneity-responsive prodrug nanocapsules for cancer chemotherapy, Adv. Mater. 25 (2013) 3670–3676.
[68] F. Bellanti, A.R.D. Coda, M.I. Trecca, A. Lo Buglio, G. Serviddio, G. Vendemiale, Redox imbalance in inflammation: the interplay of oxidative and reductive stress, Antioxidants 14 (2025) 656.
[69] P. Chen, W. Yang, K. Nagaoka, G. Lo Huang, T. Miyazaki, T. Hong, S. Li, K. Igarashi, K. Takeda, K. Kakimi, K. Kataoka, H. Cabral, An IL-12-Based nanocytokine safely potentiates anticancer immunity through spatiotemporal control of inflammation to eradicate advanced cold tumors, Adv. Sci. 10 (2023) 2205139.

[70] P. Chen, S. Li, K. Nagaoka, K. Kakimi, K. Kataoka, H. Cabral, Nanoenabled IL-15 superagonist via conditionally stabilized protein-protein interactions eradicates solid tumors by precise immunomodulation, J. Am. Chem. Soc. 146 (2024) 32431–32444.
[71] P. Chen, G. Hu, H. Cabral, Synthesis of poly(amino acids) using ring opening polymerization, Methods Mol. Biol. (2025) 241–248.
[72] R.H.H. Lu, J. Krishna, Y. Alp, S. Thayumanavan, Polymeric lysosome-targeting chimeras (PolyTACs): extracellular targeted protein degradation without Co-Opting lysosome-targeting receptors, J. Am. Chem. Soc. 148 (2026) 1259–1270.
[73] M. Iwai, C.G. Pack, Y. Takenaka, Y. Sako, A. Nakano, Photosystem II antenna phosphorylation-dependent protein diffusion determined by fluorescence correlation spectroscopy, Sci. Rep. 3 (2013) 2833.
[74] Structure of Human Serum Albumin, *Protein Data Bank* 6M4R, 2021.
[75] B. Hess, H. Bekker, H.J.C. Berendsen, J.G.E.M. Fraaije, LINCS: a linear constraint solver for molecular simulations, J. Comput. Chem. 18 (1997) 14631472.